Development of a UV Source Based on Frequency Quadrupling of a Q-switched Nd:YAG laser

ÖZLEM GÜREL

Development of a UV Source Based on Frequency Quadrupling of a Q-switched Nd:YAG Laser

Özlem Gürel

Master of Science Thesis

Laser Physics
Department of Applied Physics
School of Engineering Science
KTH

Stockholm, Sweden 2009

Contents

Abstract

In this master thesis project, a pulsed 236 nm light source operating in the UV spectral region was designed and constructed. A passively Q-switched quasi-three level Nd:YAG laser operating at 946 nm was first constructed to act as the fundamental source. Through an extra-cavity frequency doubling process using PPKTP and BiBO crystals, laser emission of 473 nm was produced with conversion efficiencies of 8.4% and 26% respectively. Using a second single pass configuration through a BBO crystal, UV emission was produced where 2.4 mW average power was obtained.

Acknowledgments

Chapter 1: Introduction

1.1 Background

After the construction of the first working laser in 1960 by Theodore Maiman[1] the development of new lasers having different properties followed fast. A year later second harmonic generation was demonstrated by P. Franken et al[2] which was also the first experiment on optical frequency conversion. By 1962 Q-switching was independently discovered and demonstrated by R.W. Hellwarth and F.J. McClung using electrically switched Kerr cell shutters in a ruby laser [3]. The first working Nd:YAG laser, which still remains the most versatile and commonly used solid-state laser, was demonstrated by Geusic *et al.*[4] at Bell Laboratories in 1964. The pace of progress is a sure indication of how fast laser advances progressed in the short time after its invention.

Today lasers comprise an important and irreplaceable part in a variety of applications in industrial, medical as well as scientific fields. Lasers operating in the UV spectral range represent one of the fastest growing segments of the laser market today, since their application extends to various fields. Some examples for applications that utilize UV lasers are as follows: Scientific uses include ultraviolet spectroscopy, nonlinear spectroscopy, remote sensing and pollution monitoring materials. Industrial applications include semiconductor fabrication systems, thin film deposition, precision micro-machining and micro-lithography.

For many years the only sources for UV radiation were gas lasers, however these lasers have drawbacks as they have limited reliability, high power consumption, and high cost. Recent developments in solid-state laser technology have allowed the production of reliable UV lasers with high powers and excellent mode quality. Using multiple nonlinear frequency processes for obtaining lasers working in the UV spectral range, is becoming a common technique. The crystals used for this purpose however, have low nonlinear coefficients leading to low powers, so in order to obtain increased power and performance, pulsed solid-state lasers operating in the infrared range are frequently utilized. This enables the production of higher peak powers hence making it suitable for efficient nonlinear frequency conversion.

1.2 Objective

The objective of this thesis was to design and construct a solid-state laser operating at 236 nm, corresponding to the UV spectral range, by means of frequency quadrupling. As the fundamental laser, an Nd:YAG laser operating at 946 nm was constructed and later Q-switched for pulsed operation using Cr^{4+}:YAG as a saturable absorber. For generation of blue light at 473 nm, frequency doubling in BiBO cut for type-I phase-matching and periodically poled KTP (PPKTP) with a nominal grating of 6.09 μm designed for first

order quasi-phase matching at 22 $^{\circ}$C was investigated. The output emission at 476 nm was frequency doubled a second time using a BBO crystal cut for type-I phase-matching. The work was carried out at KTH, The Royal Institute of Technology, Stockholm, with the courtesy of the Laser physics research group.

1.3 Outline

The outline of this thesis is as follows: In Chapter 2 background information about laser theory will be presented together with Gaussian beam properties. Chapter 3 will present an overview on the theory of solid-state lasers. Chapter 4 is intended to establish a general knowledge of the field of nonlinear optics. Chapter 5 is combined with experimental results together with supporting theoretical concepts. I will finally conclude my work in Chapter 6.

Chapter 2: Laser Basics

Lasers are devices which create and amplify light in the form of confined, intense, coherent beam. The word laser is actually an acronym for **L**ight **A**mplification by **S**timulated **E**mission of **R**adiation, which marks out the principles of operation. However the term 'light amplification' should be understood broadly since different lasers can amplify radiation at wavelengths covering the infrared, visible, ultraviolet all the way to the X-ray regions of the spectrum. The basis of the laser theory is the process of stimulated emission which is responsible for the amplification of light. Stimulated emission is a quantum mechanical phenomenon in which photons of the same frequency, phase and direction are emitted. These properties of the emitted photons attribute for the coherent property of the laser light. In this chapter the basic principles underlying the operation of a laser device will be given.

2.1 Interaction of Radiation with Matter

2.1.1 Spontaneous Emission, Absorption and Stimulated Emission

Laser principles can be best understood by first investigating the energy transition phenomenon in atoms and molecules caused by the interaction of matter with light. The three fundamental radiation processes that result from such interactions of relevance to laser physics are:

- Spontaneous emission
- Absorption
- Stimulated emission
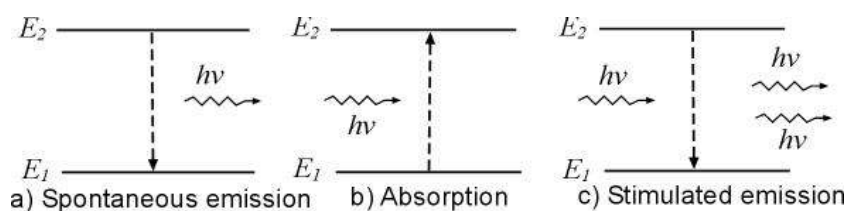
Figure 2.1 Schematic illustrations of interactions between an atom and a photon

According to quantum mechanics, atomic systems can exist only in discrete energy states where lower states are more stable than higher energy states. Therefore when an electron is in an excited state it must eventually decay to a lower level. This can either happen through non-radiative decay, where energy is released in another form than electromagnetic radiation (e.g. phonons), or radiative decay which results in the emission of a photon where the frequency v of the emitted photon is given according to Bohr's frequency relation as:

$$E_2 - E_1 = hv \tag{2.1}$$

Here a simplified 2 level model is assumed where E_2 and E_1 are the discrete energy levels and h is Planck's constant. This process is also called spontaneous emission and the photon resulting from this process has random phase and direction. When instead an atomic system interacts with electromagnetic radiation of frequency v_{21} matching the energy gap of the system, there is a finite probability that the atoms or molecules in lower energy levels will be raised to higher energy levels through a process called absorption. A laser however is based on the concept of stimulated emission in which case an atom initially in a higher energy level E_2 is stimulated by a photon, causing it to decay to the lower energy level E_1. As a result of this process a photon having the exact same frequency, direction and phase of the incident photon is emitted. When a photon with energy hv is incident on an atomic system there is an equal chance of it being absorbed by a ground-state atom or being amplified through stimulated emission. However, for the laser to operate stimulated emission should outnumber the amount of absorption and spontaneous emission processes taking place. In thermal equilibrium this is not possible since the population of the ground-state is much higher than the population of the higher energy levels. In order to create a system which favors stimulated emission there has to be more excited state atoms then ground-state atoms. This is called population inversion. However, before going into more detail the concept of Einstein's A and B coefficients will be introduced in order to get a better understanding of this concept.

2.1.2 Einstein's Coefficients

In the beginning of the century Planck described the spectral distribution of thermal radiation of a blackbody in relation with temperature T in thermal equilibrium. This relation known as Planck's law can be expressed as:

$$\rho(v) = \frac{8\pi hv^3}{c^3} \frac{1}{e^{\frac{hv}{kT}} - 1} dv \tag{2.2}$$

where $\rho(v)$ is the radiation density per unit frequency (J·s/cm^3), k is the Boltzmann constant and c is the velocity of light. In such a system in thermal equilibrium the population of any two energy levels E_i and E_j, at positive temperatures, is described by the Boltzmann Ratio as:

$$\frac{N_j}{N_i} = \frac{g_j}{g_i} \exp\left(-\frac{(E_j - E_i)}{kT}\right) \tag{2.3}$$

Here k is the Boltzmann constant and T is the absolute temperature of the material. As T increases the number of atoms in the higher energy state N_j increase. However, it can never exceed that of the lower state N_i as long as thermal equilibrium is maintained. Einstein used the Boltzmann statistics together with elements of Bohr Theory in deriving

the Planck's law where he used the concepts of absorption, spontaneous emission and stimulated emission mentioned in the previous section. As a result he derived the famous Einstein's A and B coefficients. Let us consider an idealized model of a two level system and its interaction with electromagnetic radiation in thermal equilibrium. This system can be assumed to have two non-degenerate energy levels E_1 and E_2 having populations N_1 and N_2 respectively where the total number of atoms in these levels are $N_{tot} = N_1 + N_2$. The three types of interactions of such a system with electromagnetic radiation then can be described as follows:

Absorption: The interaction of electromagnetic radiation of frequency v_{21} with an atomic system having an energy gap hv_{21} will cause the population of the lower level E_1 to decay at a rate proportional to the initial population of the level N_1 and the radiation energy density according to the following expression:

$$\frac{dN_1}{dt} = -B_{12} \cdot \rho(v) \cdot N_1$$

(2.4)

Here B_{12} is a constant with dimensions $cm^3/(s \cdot ^2 J)$ and is also referred to as Einstein's B coefficient. The rate of depopulation of level 1 in this case not only depends on the particular transition but also on the intensity of the incident wave.

Spontaneous emission: An atom raised to the upper level by absorption will eventually decay back to the lower level E_1 at a rate proportional to upper level population N_2:

$$\frac{dN_2}{dt} = -A_{21}N_2$$

(2.5)

Here A_{21} is a constant of proportionality which has dimensions s^{-1} and is also called Einstein's coefficient A. The inverse of A_{21} is $\tau_2 = A_{21}^{-1}$ which is the lifetime for spontaneous radiation of level 2.

Stimulated emission: Emission caused by the interaction of electromagnetic energy with frequency v and the atomic system will cause the population of the upper level to decrease with a rate proportional to the initial population of level 2 and the energy density of the stimulating radiation. This can be expressed as:

$$\frac{dN_2}{dt} = -B_{21} \cdot \rho(v) \cdot N_2$$

(2.6)

When the three equations obtained for absorption spontaneous emission and stimulated emission are combined the resulting rate equation for a two level system is given as follows:

$$\frac{dN_1}{dt} = -\frac{dN_2}{dt} = -B_{12} \cdot \rho(\nu) \cdot N_1 + A_{21}N_2 + B_{21} \cdot \rho(\nu) \cdot N_2$$

(2.7)

In thermal equilibrium the number of transitions from level 1 to 2 should be equal to that of level 2 to 1:

$$\frac{dN_1}{dt} = -\frac{dN_2}{dt} = 0$$

(2.8)

So equation (2.7) can be solved for $\rho(\nu)$ as:

$$\rho(\nu) = \frac{A_{21}N_2}{B_{12}N_1 - B_{21}N_2}$$

(2.9)

Using the Boltzmann ratio in Eq.2.3 gives:

$$\rho(\nu) = \frac{A_{21}/B_{21}}{\left(\frac{g_1}{g_2}\right)\left(\frac{B_{12}}{B_{21}}\right)e^{(h\nu/kT)} - 1}$$

(2.10)

Eq.2.10 and Eq.2.2 have familiar forms as they are both concerned with radiation in thermal equilibrium. So comparing the two expressions, we obtain the Einstein's coefficients:

$$\frac{A_{21}}{B_{12}} = \frac{8\pi h\nu^3}{c^3}$$

(2.11)

$$B_{12} = \frac{g_2}{g_1}B_{21}$$

(2.12)

2.1.3 Gain and Absorption

Let us consider a thin slab of thickness dz, illuminated by photons with intensity I in order to derive expressions for gain and absorption.
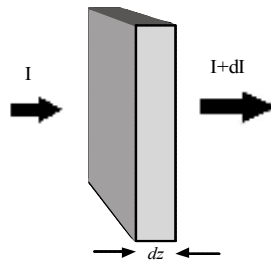

Figure 2.2 The elemental change dI in the incident intensity I after passage through a thin slab with thickness dz.

16

It is also assumed that this material has an absorption cross section σ_{ij} which is a measure of the probability of an atom to be excited to a higher energy state E_j. Similarly the probability of an atom decaying to a lower energy level E_i is expressed by the stimulated emission cross section σ_{ji}. The power emitted or absorbed from one atom is then given by $I \cdot \sigma$. If all of the atoms in the slab are taken into account the total intensity absorbed and the total intensity emitted back to the wave will be given as $N_i \cdot \sigma_{ij} \cdot dz \times I$ and $N_j \cdot \sigma_{ji} \cdot dz \times I$ respectively. Here N_i and N_j represents the population densities which are the population numbers per volume of the levels i and j respectively. The net change in the intensity in this case is:

$$dI = (N_j \cdot \sigma_{ij} - N_i \cdot \sigma_{ji}) \cdot I \cdot dz \tag{2.13}$$

Here non-radiative and radiative terms were not considered since the former process does not add photons and the photons created in the latter process are emitted in random directions giving negligible contribution to the incoming photon flux. It should also be noted that the relation between the cross sections of the absorption and the stimulated emission processes is given by [5]:

$$g_j \cdot \sigma_{ji} = g_i \cdot \sigma_{ij} \tag{2.14}$$

where g_i and g_j are the degeneracy factors of energy levels E_i and E_j respectively. The net growth in intensity as it passes through the slab of length dz can then expressed as:

$$\frac{dI}{dz} = \sigma_{ji} \left(N_j - N_i \frac{g_j}{g_i} \right) I \tag{2.15}$$

The above equations show that for the material to behave like an amplifier the condition $N_j > g_j/g_i \cdot N_i$ should be satisfied. However, in thermal equilibrium, the number of atoms in the upper levels is very small compared to that of lower levels according to Boltzmann ratio given earlier in Eq.2.3. In this case $N_j < N_i \cdot g_j/g_i$, therefore the material acts as an absorber rather than an amplifier. In order to achieve lasing, a population inversion in the material has to be created where the population of the higher energy level exceeds the population of the lower energy level. Solving Eq.2.15 gives:

$$I(z) = I(0)\exp\left(\sigma_{ji} . \Delta N . z \right) \tag{2.16}$$

where $\Delta N = N_j - N_i \, g_j/g_i$ and is called the population inversion density. When $\Delta N < 0$ as mentioned above, there is a net power absorption in the medium and an absorption coefficient can be defined as:

$$\alpha = \left(\frac{g_j}{g_i} N_i - N_j \right) \sigma_{ji} \tag{2.17}$$

In the case where ΔN > 0 the intensity of the passing photon flux grows with a gain coefficient given as:

$$g = \Delta N \sigma_{ji}$$

(2.18)

2.1.4 Atomic lineshapes

In the calculations carried out in the previous sections, the energy levels of atoms were treated as if they were sharp distinct states of clearly defined energy and also the incident wave on such a system was considered to be monochromatic. However in reality energy states are broadened over a finite range of energies. The broadening of the energy states will lead to a smear in the range of frequencies emitted introducing the concept of atomic lineshape function $g(v)$. In addition to this the incident wave will also have a bandwidth of dv. For simplicity however let us consider the interaction of a monochromatic radiation field with a transition between two energy states whose center frequency is near the frequency of the incident field. This case can be depicted as below:
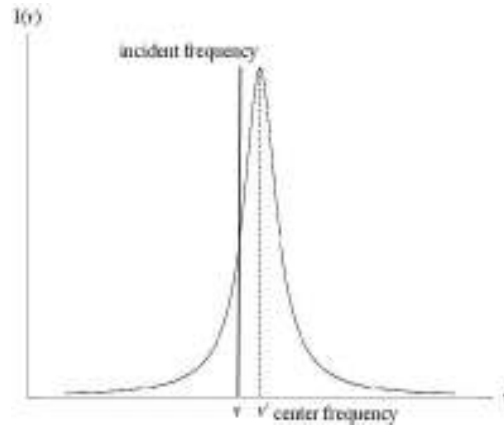
Figure 2.3: Interaction of a monochromatic field with a homogenously broadened lineshape

Here v represents the frequency of the incident monochromatic field whereas v' is the center frequency of the transition. The number of transitions taking place will increase as v gets closer to v'. The lineshape function of an atomic transition depends on the type of broadening which can be classified into two types: homogenous broadening and inhomogenous broadening. In the first case the atoms are indistinguishable and every atom has the same atomic lineshape so that the incident wave has the same effect on each atom. This type of broadening leads to a Lorentzian distribution of emitting frequencies where all of the atoms in the upper level have an equal probability in making a transition at any frequency v of that emission linewidth. Natural broadening, collision broadening and thermal broadening can be considered examples for such a process. In an Nd:YAG crystal, the main line broadening mechanism is thermal broadening. In this type of mechanism the thermal vibrations of the lattice surrounding the active ions influence the atomic transition. In the inhomogeneous broadening mechanism the atoms are distinguishable and the emission frequencies differ from particle to particle. In this case

the center frequencies of individual atoms are shifted such that the overall lineshape is broadened without broadening the individual response of the atoms. This type of broadening leads to a Gaussian distribution of emitting frequencies where specific portions of the population density of the upper level contribute to different portions of the emission linewidth. Examples are Doppler broadening and broadening due to crystal inhomogeneities.

2.2 Beam Propagation

2.2.1 Properties of Gaussian beams

A laser beam of the simplest form is the fundamental or TEM_{00} mode. A beam operating in the TEM_{00} mode has a Gaussian intensity profile where the decrease of the field amplitude with distance r from the axis is given as follows:

$$E(r) = E_0 \cdot \exp\left(-\frac{r^2}{w^2}\right)$$

(2.19)

The beam radius denoted as ω, which is commonly called spot size, is given by the radial distance at which the power density drops to $1/e^2$ of its maximum value. Hence a Gaussian beam contains 86.4% of its total power within $r = \omega$. The beam radius will have its minimum value at the beam waist denoted by ω_0.
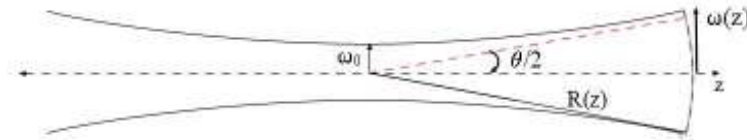
Figure 2.4 Illustration of the beam waist ω_0 for a Gaussian beam where the beam divergence is given by $\theta/2$.

For a Gaussian beam the spot size a distance z from the beam waist is given by:

$$w(z) = w_0 \left[1 + \left(\frac{z}{z_R}\right)^2\right]^{\frac{1}{2}}$$

(2.20)

where $z_R = \pi\omega_0^2 / \lambda$ is known as the Rayleigh range. The beam within a distance twice the Rayleigh range can be considered collimated. At larger distances the spot size increases linearly with z and the beam diverges at a constant angle given by:

$$\frac{\theta}{2} = \frac{\lambda}{(\pi \cdot w_0)}$$

(2.21)

The wave has plane wavefronts at the beam waist (i.e. $z = 0$) whereas at large distances the wavefronts become spherical in which case the radius of curvature can be expressed as:

$$R(z) = z \left[1 + \left(\frac{\pi \omega_0{}^2}{\lambda z} \right)^2 \right]$$

(2.22)

A Gaussian shaped beam is also referred to as diffraction limited beam since it can be focused to the smallest spot size. However it is not always the case that the beam profile is Gaussian shaped. In many lasers, modes with rectangular symmetry arise where their intensity distribution is given as [6]:

$$I_{mn}(x, y) = I_0 \left[H_m \left(\frac{\sqrt{2}x}{\omega} \right) \exp \left(-\frac{x^2}{w^2} \right) \right]^2 \left[H_n \left(\frac{\sqrt{2}y}{\omega} \right) \exp \left(-\frac{y^2}{w^2} \right) \right]^2$$

(2.23)

Here $H_m(x)$ is the mth order Hermite polynomial and ω is the spot size. The different intensity distributions result in the formation of transverse electromagnetic (TEM_{mn}) wave patterns across the beam characterized by the two indices m and n. These indices indicate the number of zeros of the field along the x any axes, respectively. The TEM_{00} mode mentioned above results when m = n = 0.
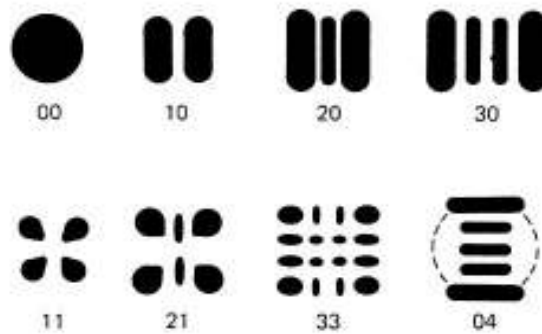

Figure 2.5. Examples for transverse mode patterns [7]

2.2.2 Gaussian Beam Propagation Using ABCD Matrices

In the previous section the properties of Gaussian beams were introduced. This section will deal with the characteristics of such beams propagating through optical media. The ABCD method offers a technique of investigating the propagation of Gaussian beams through optical elements. In order to get an understanding of this concept let us assume a lowest order Gaussian beam having a spot size ω_0 at a reference plane $z = 0$ where the beam has a planar wavefront (i.e. $R = \infty$). Suppose that this beam encounters an optical system at position z_1, referenced to the position of the beams waist as illustrated in Figure 2.6:
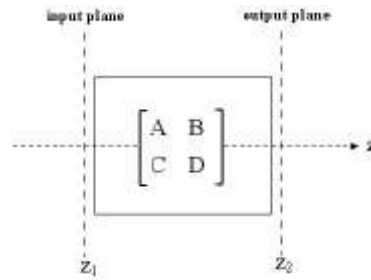
Figure 2.6. Optical system described by the ABCD matrix where the field profile at input plane z = z₁ is known.

An important property of a Gaussian beam is that after its passage through the optical elements represented by ABCD, it preserves its Gaussian nature. When such a beam passes through a lens, mirror or dielectric interface, its diameter is unchanged. However, the wavefront curvature is modified, resulting in new values of waist position and waist diameter on the output plane z_2. The ABCD matrix can be used in finding the parameters that have changed, however $\omega(z)$ and $R(z)$ do not transform in matrix fashion. The Gaussian beam in this case can be viewed as a spherical wave of complex radius of curvature q, known as the complex beam parameter. This parameter can be defined as:

$$\frac{1}{q(z)} = \frac{1}{R(z)} - i\frac{\lambda}{\pi n \omega^2(z)}$$

(2.24)

where $\omega(z)$ and $R(z)$ are expressed as given before in Eq.2.20 and Eq.2.22 respectively and λ is the wavelength of the radiation in the medium in which the beam is propagating. If $R(z)$ and $\omega(z)$ are known at z_1 the beam parameter q_1 can be calculated. With q_1 known ABCD matrix can be utilized to calculate q_2 at the output plane z_2 using the below relationship:

$$q_2 = \frac{Aq_1 + B}{Cq_1 + D}$$

(2.25)

This law is known as the ABCD law of Gaussian beam propagation. Writing q_2 in a form comparable to Eq.2.24 we obtain the following expression:

$$\frac{1}{q_2} = \frac{C + D\left(\frac{1}{q_1}\right)}{A + B\left(\frac{1}{q_1}\right)}$$

(2.26)

Equating Eq.2.24 with Eq.2.26 gives information about the beam waist and the radius of curvature of the modified beam. If the system has a sequence of optical elements, which are described by matrices $A_1, A_2, \ldots, A_N$ this is equivalent to a single optical element of the transmission matrix: $A = A_N \ldots A_2 \cdot A_1$
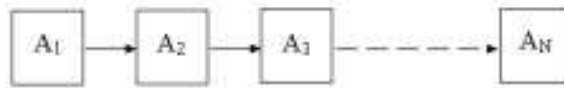
Figure 2.7. Sequence of optical elements

2.2.3 Beam Quality Factor M^2

When higher order transverse modes are present the parameters associated with the propagation of a Gaussian beam are no longer applicable to a laser beam operating multi-mode. The M^2 parameter, also called the beam quality factor, is a measure of how close a multi mode beam is to a Gaussian beam. The minimum waist and the beam divergence for such a beam can be described as follows respectively:

$$W_0 = M \cdot \omega_0$$

(2.27)

$$\Theta = M \cdot \theta$$

(2.28)

Using Eq.2.27 and Eq.2.28 together with Eq.2.21 the relation between the beam waist and the divergence angle for the real wave can be defined as:

$$\frac{\Theta}{2} = M^2 \frac{\lambda}{\pi \omega_0}$$

(2.29)

An ideal Gaussian beam has $M^2 = 1$ hence as M^2 grows beam waist and divergence increases and the beam quality drops.

2.2.4 The Knife-edge technique

A common method to measure the M^2 value is the knife-edge method [8] for which the setup can be depicted as given in Figure 2.8.
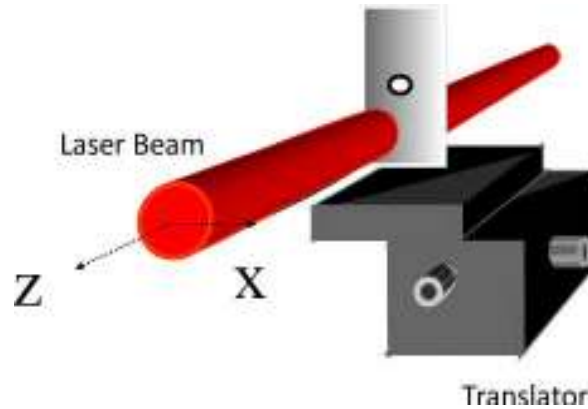
Figure 2.8. Illustration of the setup for M^2 measurement using the knife edge technique.

In this technique a lens is utilized to focus the laser beam into a tight spot with beam waist ω_0 and total divergence Θ. After measuring the total power of the beam with a power meter, a knife edge (razor in this case), which is mounted on a rail, is placed in front of the beam path at the focus, partly blocking the beam. Since the spot size is given by the radial distance at which the power density drops to $1/e^2$ of its maximum, the beam radius is measured as the distance between the points at which the power is 84% of its maximum value to where it drops to 16% of its original value. The razor is than advanced in the $+z$ direction in small increments and the same measurements are repeated up to a point where $z \gg z_0$. With the data obtained, a figure similar to Figure 2.4 can be plotted from which the divergence angle Θ can be obtained. With ω_0 and Θ known the M^2 value can be calculated using Eq. 2.29.

Chapter 3: Solid-State Lasers

A laser basically consists of three essential elements. In the simplest case it can consist of a fluorescent medium called the active element, placed in to an optical cavity composed of two mirrors facing each other and a pumping mechanism. In doing this one mirror is chosen to be partially transparent where both the mirrors are aligned parallel to each other and perpendicular to the axis of the rod.
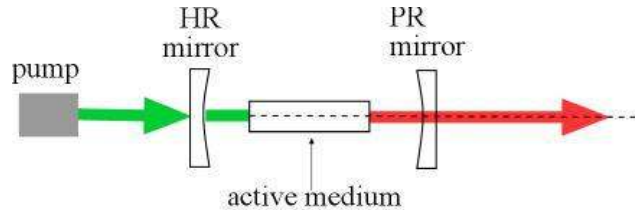

Figure 3.1 Schematic view of an optical cavity

If the light passing through the active medium is amplified by stimulated emission defined in the previous chapter such that it exceeds absorption, a powerful highly directional beam propagating along the axis can be obtained.

3.1 Gain

The active medium is responsible for the gain within the laser. It is a material comprised of a collection of atoms, molecules, or ions which has sharp fluorescent lines, strong absorption bands long, radiative lifetimes and reasonably high quantum efficiency for the fluorescent transition of interest. As the active medium, solid-state lasers utilize solid crystalline materials or glasses doped with rare earth elements or transition metal ions. It is desirable for the host to have good optical, thermal and mechanical properties. In this thesis an Nd:YAG crystal was utilized so in the following section further detail about this crystal will be given.

3.1.1 Nd:YAG lasers

Neodymium doped yttrium aluminum garnet (Nd:YAG) is a commonly used active medium due to the numerous favorable properties it possesses. It is obtained by replacing about 1% of the Y^{3+} ions in the colorless $Y_3Al_5O_{12}$ (yttrium aluminum garnet) crystal with Nd^{3+} ions. The YAG host has high thermal conductivity, is hard and is optically isotropic leading to good optical quality. Moreover the cubic structure of YAG favors a narrow fluorescent linewidth resulting in high gain and low threshold for laser operation. The YAG host used in this thesis has a monocrystalline form and was grown using the Czochralski growth method. Ceramic hosts having polycrystalline structure are also available. The main laser transition in Nd:YAG occurs between the upper Stark level of the $^4F_{3/2}$ manifold referred to as R_2 and a Stark level within the $^4I_{11/2}$ manifold at 1064 nm as shown in Figure 3.2.
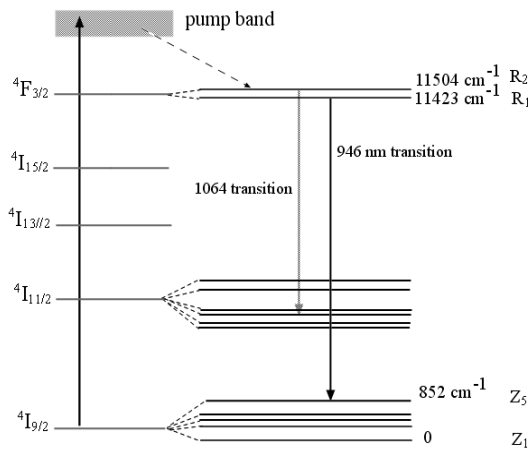
Figure 3.2 Energy level scheme of Nd.YAG showing both the 1064 nm and the 946 nm line.

In this four level system, when pumped with light at 808 nm, the active Nd^{+3} ions are excited from the ground-state to the absorption band. This is then followed by a rapid relaxation via multi-phonon emission through non-radiative processes to the upper metastable laser level R_2 in the $^4F_{3/2}$ manifold. The $^4F_{3/2}$ level is split into two Stark levels R_1 and R_2. These levels are closely coupled and hence their populations exist in a Boltzmann distribution. Lasing takes place from R_2, however its population is replenished by thermal transition from R_1 until both levels are depleted. As the transition occurs to the lower laser level a photon is emitted. From there ions will again go through rapid relaxation to the ground-state which is the $^4I_{9/2}$ level in Figure 3.2. The lower laser level is 0.26 eV above the ground-state so there is no significant thermal population in the lower laser level at room temperature. This makes the pumping threshold low and easy to obtain for a four-level Nd:YAG laser.

3.1.2 Lasing on the 946 nm transition

Lasing can also be obtained in a quasi-three level scheme where the lower laser level is so close to the ground-state that it is thermally populated at room temperature. In this case the lower laser level is a sublevel of the ground level. Since all the ground-state sublevels are strongly coupled, their populations are distributed according to the Boltzmann distribution function at room temperature. As this thesis is based on the 946 nm transition of the quasi-three level Nd:YAG laser let us consider this specific case. The diode-pumped quasi-three level Nd:YAG laser operating at 946 nm was first realized by Fan and Byer[9]. In this quasi-three level scheme the ions are excited from the ground-state into the pumping band and then very rapidly decay via radiationless relaxations down to the lowest Stark level of the energy state $^4F_{3/2}$. From here the laser transition takes place to the highest stark level of the $^4I_{9/2}$ energy state, resulting in the emission of a photon. However, achieving lasing at 946 nm is considerably more difficult than the 1064 nm line mainly due to two reasons: The first one arises from the quasi-three level nature of the system. Since the energy separation between the lower laser level and the ground-

state is comparable to *kT* there will be a considerable amount of population in level 1 leading to a significant reabsorption loss at room temperature. Another reason arises from the fact that the stimulated emission cross section is much smaller than that of the 1064 nm line. As a result the threshold for the 946 nm Nd:YAG laser is much higher than that compared to a 1064 nm Nd:YAG laser.

3.2 Optical Resonator

In general the passage of a beam once through the active medium is not sufficient in obtaining significant amplification. To overcome this problem, suitable optical feedback elements are utilized at each end of the medium in order to increase the overall amplification. In the simplest case two highly reflecting optical mirrors, one of which is partially transmitting are placed at both ends of the medium. The purpose of these mirrors is to increase the effective length of the system in order to enable the passage of the optical beam several times through the gain medium. The mirrors together with the active medium comprise an optical oscillator.

3.3 Pumping Mechanism

Pumping is the process in which atoms are raised from a lower level to a higher quantum mechanical energy levels in order to obtain gain in the cavity. It generates a population inversion in the laser medium that strongly deviates from the Boltzmann Distribution function which exits for systems in thermal equilibrium. Solid-state lasers are typically optically pumped via incoherent sources or laser diodes. However today it is more favorable to employ diode lasers as pump lasers as they provide improved beam qualities, increased system efficiencies, increased component lifetime and compact versatile setups compared to incoherent sources. Solid-state lasers pumped with such lasers are called diode-pumped solid-state (DPSSL) lasers.

3.3.1 Rate Equations for a Quasi-three level laser

As mentioned earlier the pumping process allows a mechanism for the excitation of atoms from the lower energy level to the pump band. Let us consider a quasi-three level system. In this case the number of atoms per unit volume raised to the pump level by the pumping process can be expressed as:

$$\frac{dN_3}{dt} = W_p(N_0 - N_3) \cong W_p N_0$$

(3.1)

where W_p is the pumping transition probability and N_0 is the population density of the ground-state. Here it has been assumed that the population density of the upper state N_3 is much lower than that of the ground-state N_0. The number of atoms per unit volume which reaches the upper laser level is given by:

$$R_p = \eta_p W_p N_0$$

(3.2)

R_p in this case is the effective pump rate where η_p represents the pump efficiency. As mentioned earlier the lower level is a sublevel of the ground-state in a quasi-three level laser. In addition the upper laser level may also be a sublevel of level 2. In this case let us denote the total population densities of all the sublevels of the lower and upper energy levels as N_1 and N_2, respectively. Since the separation between the ground level and the upper laser level is comparable to kT there will be a considerable amount of population in level 1 of the system. Assuming decay from the absorption band to upper laser level 2 is rapid we can approximate $N_3 = 0$ hence $N_T = N_1 + N_2$ where N_T is the total population density. In this case the rate equations and photon density concerning a quasi-three level laser can be formulated according to[10]:

$$\frac{dN_2}{dt} = -\frac{dN_1}{dt} = R_p - c_0 \sigma_{21} \phi \Delta N - \frac{N_2}{t_2}$$

(3.3)

$$\frac{d\phi}{dt} = c\phi\sigma\Delta N - \frac{\phi}{\tau_c}$$

(3.4)

where τ_c is the decay time for photons in the optical resonator. In Eq. 3.3 the terms on the right of the equality accounts for pumping, stimulated emission and spontaneous emission, respectively. As mentioned earlier the levels 1 and 2 consist of g_1 and g_2 sublevels, respectively. These sublevels have different energies and very fast relaxation among other sublevels of the particular level they belong to. Taking this into consideration, the population density of the upper laser level can then be written as $N_{2i} = f_{2i}N_2$ where f_{2i} is the fraction of total population of level 2 that is found in sublevel j at thermal equilibrium. According to Boltzmann statistics we can write f_{2i} as[5]:

$$f_{2i} = \frac{g_{2i} \exp\left[-\left(\frac{\Delta E_{2i}}{k_B T}\right)\right]}{Z_2}$$

(3.5)

Where Z_2 is the partition function of level 2 and can be written as:

$$Z_2 = \sum_{m=1}^{g_2} g_{2m} \exp\left[-\left(\frac{\Delta E_{2m}}{k_B T}\right)\right]$$

(3.6)

Here ΔE_{2m} is the energy difference between the mth sublevel and the lower sublevel in the upper level and g_{2m} is the degeneracy. The same logic can be applied to level 1 to obtain an expression for f_{1j}. In this case ΔN in Eq.3.3 and Eq.3.4 becomes $\Delta N = N_{2i} - N_{1j}$. Since the lower laser level is a sublevel of level 1 there is a considerable amount of reabsorption losses where photons produced by the stimulated emission process are lost to the absorption band.

3.3.2 Energy Transfer Upconversion

Energy transfer upconversion (ETU) is an energy transfer mechanism which occurs between two neighboring ions in the upper laser level. In this process energy is transferred from a donor ion to an acceptor ion. While the donor ion relaxes to a lower energy level, the neighbouring ion which accepts the energy is excited to a higher energy level than the upper laser level. The acceptor ion then returns back to lower energy levels either radiatively or non-radiatively via multi-phonon relaxation. One effect of ETU is that it reduces the population of the upper laser level thereby reducing the population inversion. This is especially important for quasi-three level lasers which have low gain values. Another consequence is the generated heat from the multi-phonon relaxations which increase the effects of thermal loading. The effect of ETU can be detrimental in Nd-doped lasers[11-16], particularly Q-switched configurations which require high upper level excitation densities. With the inclusion of ETU effects the rate equations are modified in the following way where the so-called upconversion rate parameter W is added:

$$\frac{dN_2}{dt} = -\frac{dN_1}{dt} = R_p - c_0\sigma_{21}\phi\Delta N - \frac{N_2}{t_2} - WN_2^2$$

(3.7)

For Nd:YAG, W has the value of 2.8.10-22 m^3 s^{-1}[11].
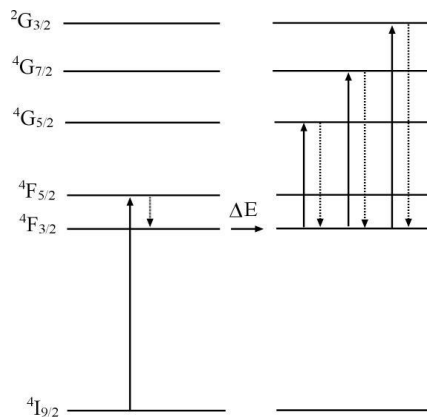
Figure 3.3 Energy level scheme of Nd:YAG depicting possible upconversion processes.

3.4 Passive Q - switching

Q-switching[17] is a common technique which allows the generation of short energetic pulses in a cavity. In order to achieve this, the cavity losses are initially kept high which in return builds up a population inversion much larger than usual, thus storing the energy in the gain medium. Then the cavity loss is suddenly lowered so that the laser will exhibit a gain much higher than the losses causing the energy stored to be released in the form of a short and intense light pulse. Passive Q-switching using saturable absorbers[18] is one of the techniques that can be utilized in obtaining such pulsed operation. As opposed to active Q-switching methods which require an external driving source to lower the

feedback in the cavity, this technique exploits the nonlinearity of an absorber for the same purpose. A saturable absorber consists of a material which absorbs at the laser wavelength and saturates as the ground-state level of the absorber is depleted. The saturable absorber becomes transparent as the intensity of the light passing through increases allowing oscillation to build up in the cavity which results in the formation of a giant pulse. After the pulse, the absorber recovers to its high-loss state allowing self modulation in the cavity. Since passive Q-switching can be realized with a relatively simple design, compared to active methods, it enables setups which are small, robust and low cost. However a disadvantage of this method is that it leads to amplitude fluctuations and timing jitter. The timing jitter can be attributed to a variety of reasons. These include pump intensity variations, changes in spatial pump properties, spontaneous emission noise, and changes in distribution of spatial modes for emission in the laser cavity.

3.4.1 Cr^{4+}:YAG as a saturable absorber

Cr^{4+}:YAG with its large absorption cross-section in the near IR, relatively high active ion concentration, moderate excited state lifetime (τ_2) and superior thermal and mechanical properties is a good candidate for passive Q-switching. The performance of Cr^{4+}:YAG has been demonstrated in several cases[19],[20],[21] for Nd:YAG lasers. In Cr^{4+}:YAG the Cr^{4+} ions provide the high absorption cross section of the laser wavelength whereas the YAG host provides the chemical, thermal, and mechanical properties required for a longlife time. The four level energy diagram of Cr^{4+}:YAG is shown below in Figure 3.4.
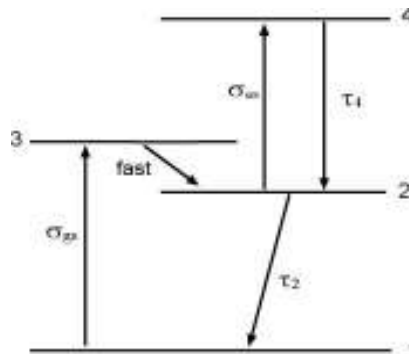

Figure 3.4. Four-level model of Cr^{4+}:YAG saturable absorber

The absorption at the wavelength of interest occurs from level 1 to 3. Considering the transition from there to level 2 is fast, if τ_2 is fast eventually the ground level will become depleted causing the material to become transparent to the laser radiation. However, in practice this transmission is never 100% because many of the materials used as saturable absorbers, including Cr^{4+}:YAG, exhibit absorption also from an excited state at the same wavelength as that which is to be Q- switched. This can be seen as the transition between levels 2 and 4 in Figure 3.4. The process in which the population at the upper laser level is excited to higher energy levels is called excited-state absorption (ESA). When the ground-state absorption in the Q-switch material has been saturated, ESA leads to a

residual loss in the resonator. Because of the fast relaxation rate of the excited level (i.e. level 4 in Figure 3. 4) ESA transition between levels 2 and 4 does not saturate so it is essential for a material to have $\sigma_{gs} > \sigma_{es}$ for it to be suitable as a saturable absorber.

Chapter 4: Nonlinear Optics

4.1 Nature of Nonlinear Polarization

When an electromagnetic wave propagates through a medium, an electric field acts on each particle displacing them from their equilibrium positions. In such a case, positively charged cores and surrounding negatively charged electrons are displaced in opposite directions. This leads to the separation of opposite charges, creating dipoles in the medium. The resultant dipole moment per unit volume can be written as:

$$P = \varepsilon_0 \left(\chi^{(1)} E_1 + \chi^{(2)} E_1 E_2 + \chi^{(3)} E_1 E_2 E_3 \ldots \right) = P_L + P_{NL}$$

(4.1)

where $\chi^{(n)}$ represents the nth order susceptibility. Here the first term describes the linear polarization whereas the higher order terms correspond to nonlinear polarization terms of second order, third order and so forth. At low intensities of the incident electrical field, the higher order terms can be neglected since $\chi^{(1)} \gg \chi^{(2)} \gg \chi^{(3)}$ etc. In this case, the optical properties of the medium such as refractive index and absorption will remain unchanged and the emitted radiation will have the same frequency as the incident light. However, as light intensity grows, the higher order terms can no longer be neglected. At such high intensity fields, the optical response of the medium to the radiation becomes nonlinear, optical properties such as refractive index and absorption become dependent on the light intensity and new light frequencies not present in the initial field can be created as it traverses the medium. Second order nonlinearity can occur only in crystal materials with a non-centrosymmetric crystal structure. Among these processes second harmonic generation (SHG), sum frequency generation (SFG) and difference frequency generation (DFG) can be given as important examples. These processes can be illustrated schematically as below:

a) SFG : $\omega_3 = \omega_1 + \omega_2$
b) SHG : $\omega_3 = \omega_1 + \omega_1$
c) DFG : $\omega_3 = \omega_2 - \omega_1$

Figure 4.1 Frequency conversion processes in second order nonlinear medium where two input photons are added or subtracted resulting in one photon of higher or lower energy.

Let us consider two waves at frequencies ω_1 and ω_2 incident on a nonlinear medium as depicted in Figure 4.1. For SFG the photon energies are added to create a photon with higher energy $\omega_3 = \omega_1 + \omega_2$. SHG is a special case of SFG, where the incident waves have the same frequencies, combining to give a photon with twice the energy. In DFG the interaction of the incoming waves creates a photon of lower energy such that $\omega_3 = \omega_1 - \omega_2$. The second term expressed in Eq.4.1 as $P^{(2)} = \chi^{(2)} E_1 E_2$ is responsible for the above mentioned processes where $\chi^{(2)}$ is a tensor of third rank consisting of 27 elements.

Often instead of the susceptibility the so called *d* coefficient is used where *d* is also a tensor given by

$$d_{il} = \frac{1}{2} X_{123}$$

(4.2)

In writing the second order polarization term, it makes no physical difference in which order the product of the field amplitudes are written. Therefore using intrinsic permutation symmetry, the tensor χ_{ijk} can be written as χ_{ikj}. Making use of this notion, the indices *j* and *k* are replaced by a single index *l* such that:

l	1	2	3	4	5	6
jk	11	22	33	23,32	13,31	12,21

With this simplification made the number of independent elements are reduced to 18, so the second order polarization matrix can be written as:

$$\begin{bmatrix} (P^{(2)}{}_{\omega_3})_x \\ (P^{(2)}{}_{\omega_3})_y \\ (P^{(2)}{}_{\omega_3})_z \end{bmatrix} = 2\varepsilon_0 K \begin{bmatrix} d_{11} & d_{12} & d_{13} & d_{14} & d_{15} & d_{16} \\ d_{21} & d_{22} & d_{23} & d_{24} & d_{25} & d_{26} \\ d_{31} & d_{32} & d_{33} & d_{34} & d_{35} & d_{36} \end{bmatrix} \cdot \begin{bmatrix} (E_{\omega_1})_x (E_{\omega_2})_x \\ (E_{\omega_1})_y (E_{\omega_2})_y \\ (E_{\omega_1})_z (E_{\omega_2})_z \\ (E_{\omega_1})_y (E_{\omega_2})_z + (E_{\omega_2})_y (E_{\omega_1})_z \\ (E_{\omega_1})_x (E_{\omega_2})_z + (E_{\omega_2})_x (E_{\omega_1})_z \\ (E_{\omega_1})_x (E_{\omega_2})_y + (E_{\omega_2})_x (E_{\omega_1})_y \end{bmatrix}$$

(4.3)

Where *K* is a degeneracy factor which is given as:

$K = 1/2$ for $\omega_1 = \omega_2$
  $= 1$ for $\omega_1 \neq \omega_2$

For the case where the material is transparent to all three frequencies ω_1, ω_2 and ω_3, Kleinman symmetry conditions[22] can be taken into account to further reduce the number of elements of the *d* coefficient.

4.2 The Coupled Wave Equations

Nonlinear effects, observed when three optical fields propagate through a medium exhibiting second order nonlinearity, can be described by the nonlinear wave equation and the second order nonlinear polarization acting as the source term. Assuming a non-magnetic medium with no free charges, the nonlinear wave equation can be derived using Maxwell's equations and can be expressed as:

$$\nabla x \nabla x E = -\mu_0 \sigma \frac{\partial E}{dt} + \mu_0 \frac{\partial^2 E}{dt^2} + \mu_0 \frac{\partial P^{2NL}}{dt^2} \tag{4.4}$$

In solving this equation analytically, if we assume plane waves travelling in the z-direction (i.e. d/dx = d/dy = 0), the electrical field and polarization of such waves can be written as below:

$$E(z, t) = \frac{1}{2}\left(E(z)e^{i(\omega t - kz)} + c.c\right) \tag{4.5}$$

$$P(z, t) = \frac{1}{2}\left(P(z)e^{i(\omega t - kz)} + c.c\right) \tag{4.6}$$

where *c.c* denotes the complex conjugate terms. If we also assume the envelope of the plane waves changes slowly in time with distance, then the second-order derivatives with respect to time can be neglected. This is called the slowly varying envelope approximation (SVEA):

$$\left|\frac{\partial^2 E(z)}{\partial x^2}\right| \ll \left|k \frac{\partial E(z)}{\partial x}\right|$$

$$\left|\frac{\partial^2 E(z)}{\partial t^2}\right| \ll \left|\omega \frac{\partial E(z)}{\partial t}\right| \tag{4.7}$$

$$\left|\frac{\partial^2 P(z)}{\partial t^2}\right| \ll \left|\omega \frac{\partial P(z)}{\partial t}\right|$$

By inserting Eq 4.5 into Eq 4.4 and taking SVEA into account Eq 4.5 can be simplified to a first order differential equation giving the below relation:

$$\frac{\partial E}{\partial z} = -\alpha E + \frac{i\mu_0 c_0 \omega}{2n} P_{NL} \tag{4.8}$$

where

$$\alpha = \frac{\mu_0 \sigma c_0}{2} \tag{4.9}$$

 is the loss coefficient in the material. For a second order nonlinear process involving the interaction of three optical frequencies ω_1, ω_2, ω_3, the induced polarizations are expressed in Eq. 4.3. Substituting this equation into Eq. 4.8, identifying d_{eff} as the effective nonlinear coefficient and taking the interacting polarization fields into account we obtain the following coupled wave equations:

$$\frac{\partial E_1}{\partial z} = -\alpha_1 E_1 + i\kappa_1 E_3 E_2^* e^{-i(k_3 - k_2 - k_1)z}$$

$$\frac{\partial E_2}{\partial z} = -\alpha_2 E_2 + i\kappa_2 E_3 E_1^* e^{-i(k_3 - k_2 - k_1)z}$$

(4.10)

$$\frac{\partial E_3}{\partial z} = -\alpha_3 E_3 + i\kappa_3 E_1 E_2 e^{-i(k_3 - k_2 - k_1)z}$$

where;

$$\kappa_i = \frac{\omega_i d_{eff}}{n_i c_0}$$

(4.11)

Here $i = 1,2,3$, n_i is the refractive index and c_0 is the velocity of light in vacuum. Also $\Delta k = k_3 - k_2 - k_2$ represents the phase mismatch between the interacting waves. Coupled wave equations in general describe how the interacting waves are coupled to one another through d_{eff} and how energy flows from one wave to another through this coupling.

4.3 Second harmonic generation

4.3.1 Plane wave analysis

In SHG, two incident waves with equal frequencies interact such that a new wave with twice the frequency is generated:

$$\omega_F + \omega_F = \omega_S \quad , \quad k_{sh} = k_3, \ k_F = k_1 = k_2 \quad (4.12)$$

If we assume the material does not absorb at the generated frequency ω_{SH} (i.e. $\alpha = 0$) and also neglecting pump depletion (i.e. $\partial E_F / \partial z = 0$) last expression in Eq. 4.10 becomes:

$$\frac{\partial E_{SH}}{\partial z} = i\kappa E_F E_F E^{i\Delta kz}$$

(4.13)

where $\Delta k = k_{SH} - 2k_F$. By integrating the above expression over the crystal length and taking into account the input intensity at the fundamental frequency ω_F is given by:

$$I_F = \frac{1}{2}\varepsilon_0 c n_F E_F E_F^*$$

(4.14)

the intensity of the second harmonic signal can be obtained from:

$$I_{SH} = \frac{2\omega^2 d_{eff}^2 L^2 I_F^2}{\varepsilon_o c^3 n_{SH} n_F^2} \sin c^2\left(\frac{\Delta k L}{2}\right)$$

(4.15)

From Eq. 4.15 we can see that the SHG intensity is proportional to the square of the input intensity for a plane wave and is maximized in the case of complete phase-matching $\Delta k = 0$. SHG reduces rapidly as the phase matching condition shifts from $\Delta k = 0$.

4.3.2 Gaussian Beam analysis

In order to maximize conversion efficiency, one usually focuses a Gaussian beam into a nonlinear crystal instead of using a plane wave. Therefore it is useful to extend the analysis to such beams with beam waist ω_0 and where the interaction length within the crystal is L. Since the intensity is given as power per unit area ($P = IA$) in order to reach higher conversion efficiencies it is desirable to use tighter focusing. It can also be seen from Eq. 4.15 that a long nonlinear crystal length is also important in achieving high intensities for the generated nonlinear frequencies. However, as the beam waist gets smaller, diffraction effects become more distinct, meaning as soon as the beam is confined to a tight spot it will spread very rapidly limiting the efficient usage of the crystal length. This means there is a trade-off between the long crystal length and the tight focusing of the Gaussian beam. Boyd and Kleinman have addressed this problem examining the case of Type I SHG using a focused Gaussian beam in a material exhibiting walk-off. This method assumes the crystal to be divided into infinitesimally small slices each corresponding to a different spot size of the incident fundamental beam. The fundamental beam in each slice will cause the generation of a second harmonic wave where the intensities of these waves will depend on the incident spot size. The idea then is to add up the contributions from each slice taking relative phases into account. If we assume a Gaussian beam focused to a beam waist ω_0 and confocal parameter $b = 2\pi n_1 \omega_0^2 / \lambda_1$ where n is the refractive index of the crystal at the fundamental wavelength the second harmonic power in such a case is[23]:

$$P_{SH} = \frac{16\pi^2 d_{eff}^2}{\varepsilon_0 c_0 \lambda_1^3 n_2 n_1} P_1^2 L h(\xi, B, \sigma)$$

(4.16)

where ω_F and k_F are the fundamental frequency and wave vector respectively, c is the speed of light in vacuum, ε_0 is the permittivity of free space $h(\xi, B, \sigma)$ is the Boyd-Kleinman focusing factor. The parameters used in this equation can be defined as:

$$\xi = L/b$$

$$B = \rho \sqrt{Lk_1}/2$$

(4.17)

$$\sigma = b\Delta k/2$$

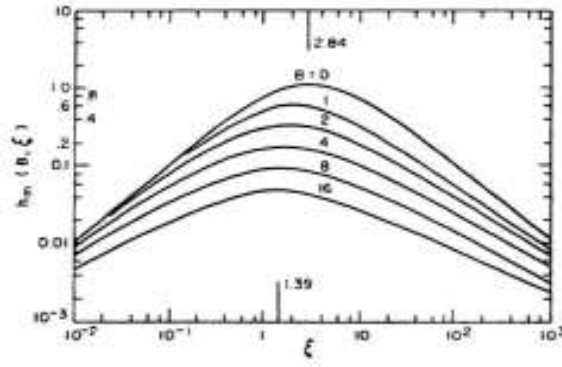Here ξ represents the degree of focusing and σ adjusts Δk in order to maximize the SH output.

Figure 4.2 Plot of the focusing factor h(ξ,B,σ) as a function of the focusing parameter ε for various values of double refraction parameter B[23].

The generated power can be maximized by optimizing the focusing function $h(\xi,B,\sigma)$ with respect to the focusing parameter ξ, the walk-off parameter B and the phase-matching parameter σ. From Figure 4.2 it can be seen that the maximum condition is reached for $B = 0$ which can be obtained in the case of non-critical phase matching where there is no walk-off.

4.4 Phase-Matching

In obtaining efficient SHG, phase-matching is a critical parameter which occurs when the phase velocities of the generated wave and the driving nonlinear polarization wave is matched. Such a phase-matching condition can be obtained when the below vector condition is satisfied:

$$\Delta k = k_{SH} - 2k_F = 2\omega/c_0(n_{SH} - n_F) = 0 \qquad (4.18)$$

However this is difficult to achieve in practice because of the optical dispersion in materials. When there is a significant amount of phase mismatch Δk, the SHG intensity exhibits an oscillatory behavior with period $L = 2\pi/\Delta k$ along the crystal. This happens in such a way that after a certain distance which corresponds to half the period, the SHG wave and the driving polarization become 180^0 out of phase and the intensity begins to flow back to the fundamental wave. This distance which equals half the period is called the coherence length:

$$L_c = \pi/\Delta k \qquad (4.19)$$

and specifies the length from the crystal entrance at which maximum SHG power is reached. Improved phase-matching allows longer coherence lengths, which in return allows utilizing a bigger portion of the useful crystal length. There are essentially two types of phase-matching techniques depending on whether the interacting waves are collinear or not. These techniques will be described in more detail in the following section.

36

4.4.1 Birefringent Phase-matching

A common method to achieve the $\Delta k = 0$ condition is the birefringent phase-matching technique (BPM), where the birefringent nature of uniaxial or biaxial crystals are employed in order to achieve equal phase velocities of the interacting waves. These types of crystals have anisotropic structures such that, along the optical axis, atoms are arranged symmetrically. Crystals having one such axis are called uniaxial. A beam polarized along this axis will experience the same refractive index regardless of propagation direction whereas a beam polarized orthogonally will experience a refractive index which varies with direction of propagation. Birefringence can be defined as the difference between these refractive indices, n_o - n_e, where n_o and n_e are the refractive indices for polarizations perpendicular (ordinary) and parallel (extraordinary) to the axis of anisotropy, respectively. The refractive index of the extraordinary wave is in general a function of the polar angle defined as θ between the optical axis and the wavevector representing the propagation direction[24] :

$$\frac{1}{n_e(\theta)^2} = \frac{\cos^2\theta}{n_o{}^2} + \frac{\sin^2\theta}{n_e{}^2}$$

(4.20)

If we assume a negative uniaxial crystal such that $n_o > n_e$, the dependences of the refractive indices of the orthogonal waves are given by a sphere with radius n_o for ordinary waves and an ellipse with semi-axes n_o and n_e for the extraordinary waves.
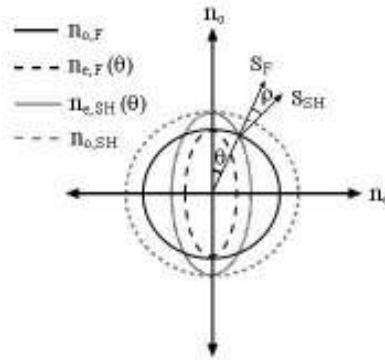

Figure 4.3 Dependance of the refractive index on light propagation direction and polarization in negative uniaxial crystals.

In such cases where an angular variation is utilized in order to achieve the phase-matching condition (i.e light enters the crystal with an oblique angle, $\theta \neq 90$) the split orthogonal waves diverge from each other leading to what is known as spatial walk-off. In this case the Poynting vectors shown as S_{SH} and S_F in Figure 4.3 become non-collinear: The angle between the fundamental and the rotated second harmonic pointing vectors, denoted by ρ, for a negative uniaxial crystal and Type I phase-matching is given by[10]:

$$\tan \rho = \frac{(n_{o,F})^2}{2} \left[\frac{1}{(n_{e,SH})^2} - \frac{1}{(n_{o,SH})^2} \right] \sin 2\theta$$

(4.21)

As a consequence of walk-off, the spatial overlap between the fundamental and second harmonic waves will be reduced after a certain propagation distance, shortening the possible interaction length. Since the aim of BPM is to increase the interaction length as long as possible, this reduction leads to lowered conversion efficiencies. This also puts limitations on beam focusability since the spatial walk-off becomes more important for smaller beam waists. The effects of spatial walk-off can be eliminated by using Non-Critical Phase-Matching where the fundamental and second harmonic waves propagate collinearly (i.e $\theta = 90$) along the optical axis. In this case beams can be focused more tightly leading to higher conversion efficiencies. NCPM can be achieved through temperature tuning.

4.4.2 Quasi-phasematching

Another method which allows matching the phase velocities of the interacting waves is the Quasi-Phase Matching (QPM) technique proposed by Armstrong et al in 1962[25] . In this method the phase mismatch is corrected by reversing the crystal orientation periodically. According to Eq. 4.15, in the non-phase matched case, the power flows back and forth between the fundamental and the SH wave with period $\Delta kL/2 = \pi$. The idea of QPM is to allow the phase mismatch along the coherence length, where the intensity of the SH field reaches a maximum value, and afterwards to reverse the nonlinear susceptibility introducing a 180^0 phase shift. In this way destructive interference is prevented and instead of flowing back from the SH wave to the fundamental wave, energy is continuously extracted from the pump and the SH field grows monotonically. In the presence of spatial modulation the nonlinear susceptibility becomes [26]:

$$d(z) = dil \sum_{m=-\infty}^{\infty} G_m \exp(iK_m z)$$

(4.22)

Here $K_m = 2\pi m / \Lambda$ where m is the order of the QPM process and Λ is the period. Also G_m is the Fourier coefficient of the mth harmonic. In this case the field of the second harmonic wave after travelling a distance L in the medium is given by:

$$E_{2\omega} = \frac{i\omega E_\omega^2}{n_{2\omega} c_0} \int_0^L d(z) e^{-i\Delta kz} dz$$

(4.23)

where E_ω is the fundamental field, $d(z)$ denotes the spatial dependence of the nonlinear coefficient, and Δk is the phase mismatch. Combining Eq. 4.22 and 4.23 one gets:

$$E_{2\omega} = \frac{i\omega E_\omega^2 d_{il}}{n_{2\omega}c_0} \int_0^L \sum_{m=-\infty}^{\infty} \sigma_m e^{-i(K_m - \Delta k)z} dz$$

(4.24)

We can see from this expression that as K_m gets closer to Δk, the second harmonic field will grow. This enhancement becomes greatest for m = 1 which is the most generally used type of QPM called first order QPM. It can be achieved by changing the orientation of the crystal every coherence length l_c. The closest value of Δk to K_m is obtained for one particular Fourier component where the corresponding Fourier coefficient is given by:

$$G_m = \frac{2}{m\pi} \sin(m\pi D)$$

(4.25)

Here D is the duty cycle determined by the ratio of the reversed domain length and the structure period Λ. The effective nonlinear coefficient is then given by: $d_{eff} = G_m d_{il}$. In this case the phase-matching condition becomes

$$\Delta k_q = k_{SH} - 2k_F - K_M$$

(4.26)

Phase-matching condition can be reached when $\Delta k_q = 0$. Since d_{eff} drops for higher m values its best to achieve phase-matching using m = 1. In this case $d_{eff} = (2/\pi).d_{il}$ and the proper period of the grating satisfying this condition is:

$$\Lambda = \frac{2\pi}{k_{SH} - 2k_F}$$

(4.27)

QPM reduces the effective non linear coefficient by factor of $2/\pi$, however, the overall conversion efficiency can be several times larger than with BPM because in this case the largest nonlinear coefficient d_{33} can be utilized. Than all waves are polarized along the polar axis which is impossible with BPM.

4.5 Damage of Nonlinear Crystals

Some nonlinear crystal materials exhibit what is known as the photochromic effect when subject to short wavelengths[27]. Aside from the loss of fundamental light, this effect also causes temperature gradients in the crystal which in turn induces refractive index changes in the material via the thermo-optic effect. As a consequence instabilities in the output power and low conversion efficiencies can be observed. Using high peak powers in combination with long crystals tends to make the photochromic effect more visible as absorption of the incident radiation grows. Furthermore photochromic effect in KTP leads to absorption of the infra-red light referred to as the blue induced infrared absorption (BLIIRA)[28]. This will have similar effects to those mentioned above for visible light absorption in addition to the decrease of fundamental power for nonlinear

conversion. The combined effects will limit the generated second harmonic power. The effects of photochromic effect decreases for elevated temperatures. For KTP it has been shown that using a temperature range of 70-100 ^{o}C reduces the photochromic effect leading to stable operation[29].

Chapter 5: Experimental Analysis

The general layout of the laser is depicted in Figure 5.1. A simple and compact linear cavity of 3.2 cm was used. Further specifications regarding the laser design will be given sequentially in the following sections.
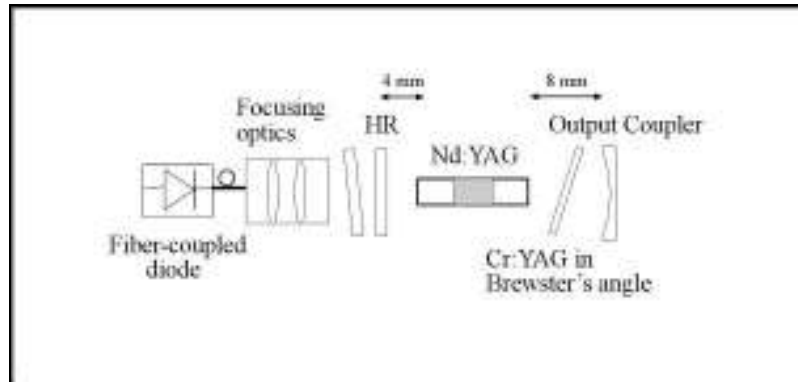
Figure 5.1 Experimental setup for the Q-switched 946-nm laser.

5.1 Pump Source

In this thesis an optical end-pump configuration was utilized. In such a system, with the right choice of focusing optics, the diode pump radiation can be made to overlap with the diameter of the laser mode reducing the waste of pump energy. This makes it possible to reach higher power efficiencies. End pumping also provides a small gain volume leading to higher beam quality in the TEM_{00} mode. In end pumped configurations, in order to obtain mode matching between pump radiation and the laser mode, tight focusing of the pump beam to a small spot size is necessary. This is usually done by using fiber coupled laser diodes as was the case in this thesis. The pump source used was a 100 μm fiber coupled laser diode (Limo GmbH) with a numerical aperture (N.A) of 0.22 emitting up to 18 watts. Initially a 200 μm fiber coupled laser diode was utilized as the pump source. However, the initial source was damaged along the progress of the thesis. The damage to the laser diode was attributed to possible back reflection from the mirrors. During the Q-switching process very high powers circulate in the system. A possible back reflection can explain the damage that occurred in the laser diode. In order to prevent this problem from repeating a protection window slightly tilted into an angle was placed into the setup (Figure 5.1). The M^2 measurement held for the pump source yielded a value of $M^2 = 58$ as the beam quality factor.
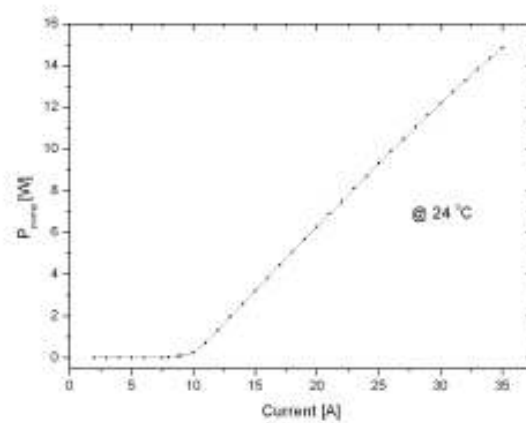
Figure 5.2 Pump power vs. driving current.

The operating wavelength of the laser diode was temperature and driving current dependant. The effect of increased temperature and current for the driver can be seen as a shift towards higher wavelengths in Figure 5.3. The emission bandwidth of the pump laser was tuned by adjusting the temperature to a value which provided optimum correspondence with 808 nm as the center wavelength over a range of current values. As a result the operating temperature of 24 $^{\circ}$C was chosen. The output from the fiber coupled laser diode was collimated and focused onto the laser crystal using two plano-convex lenses with focal lengths of 30 mm. A beam waist of approximately 50 μm was achieved 2 mm inside the laser crystal.
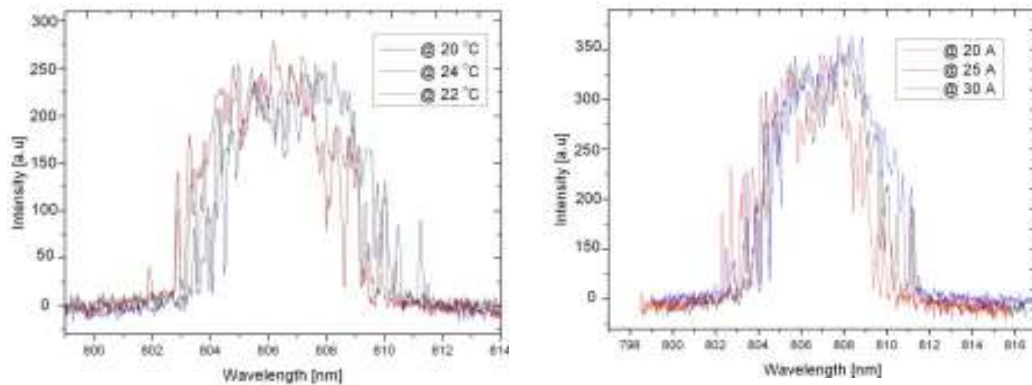

Figure 5.3 Effect of temperature change on emission bandwidth of the pump source (left) Effect of current change (right)

5.2 Laser operation at 946 nm

The laser crystal was a composite 5 mm long Nd:YAG (doping level 1.1 atm%) crystal with 5 mm long undoped YAG end caps. It had a diameter of 3 mm and was water cooled to a temperature of 13 $^{\circ}$C. Figure 5.4 shows the fluorescence spectrum of the crystal

between 940 nm and 1100 nm obtained by pumping at 808 nm. It can be seen that the 1064 nm line is clearly stronger than the 946 nm line.
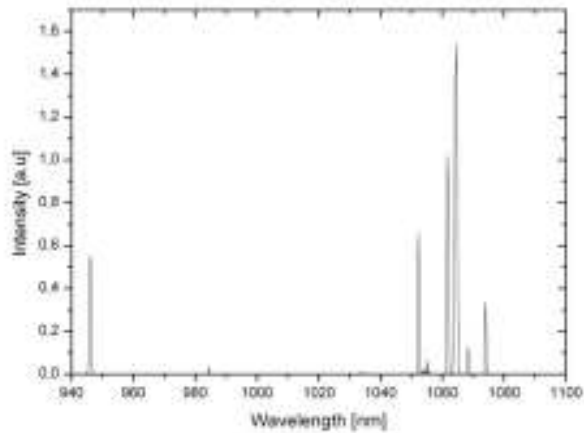

Figure 5.4 Fluorescence spectrum for the Nd:YAG crystal

In order to suppress the more dominant 1064 nm line both surfaces of the crystal were AR coated for 946 nm. As the incoupling mirror a planar mirror with HR coating for 946 nm (AR for 808 nm and 1064 nm) was used. A curved mirror (ROC = 200 mm) with a transmission value of 10% for 946 nm (AR for 1064 nm) was chosen as the output coupler. The choice of the output coupler was made experimentally after testing several mirrors with different radius of curvatures. The optimum output power (Figure 5.5) and beam quality values (Figure 5.6) were obtained with the output coupler having ROC = 200 mm.
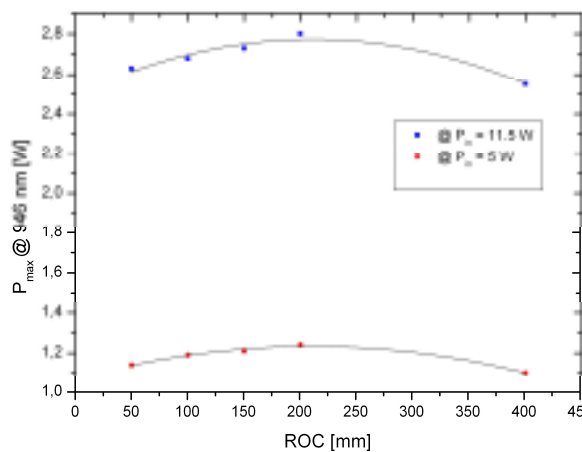

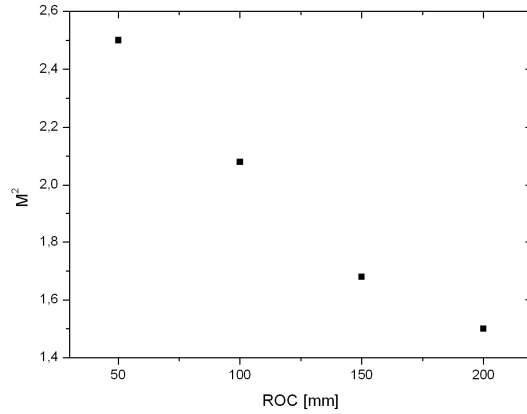*Figure 5.5 Measured output power for 946 nm vs. ROC for several output coupling mirrors.*

Figure 5.6 Measured M² values vs. ROC for several output coupling mirrors.

For 9.1 W of absorbed power an output of 1.96 W was obtained in the cw mode. The slope efficiency yielded a value of 26%.
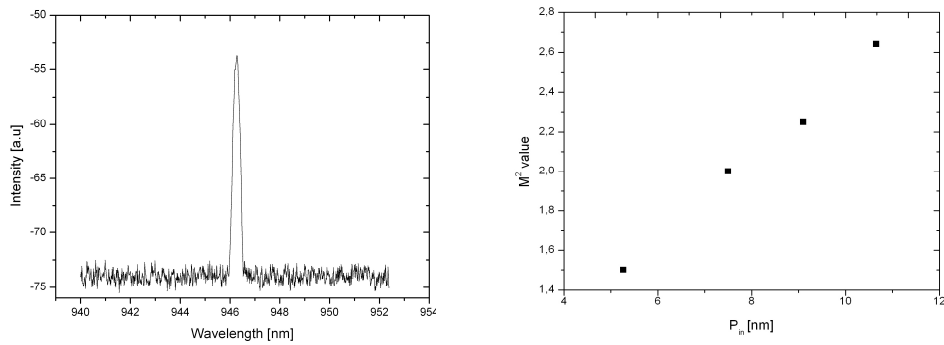

Figure 5.7 Measured emission spectrum at 946 nm (left), Absorbed power vs M² factor(right)

The corresponding beam quality obtained was $M^2 = 2.2$ Figure 5.7 plots how the M^2 value is affected by increasing the pump power where it is clear that the beam quality degrades with increased input values.

To achieve efficient operation of Nd:YAG at 946 nm is significantly more challenging than on the much higher gain 1064 nm line. The main problem arise from the need to focus the diode pump beam to a relatively small beam size due to the very low gain cross section and quasi-three level nature of the 946 nm line. High focusing causes heating which places extra demands on the beam quality of the pump source and the resonator design. It was essential to obtain good beam quality since it is an important criterion in obtaining efficient frequency conversion. The pump spot size in the crystal was adjusted to achieve reasonable compromise between output power and spatial beam quality by adjusting the crystal position. The effects of thermal loading can be seen as input powers increase and the resultant output powers loose linearity (Figure 5.8a). The crystal position was displaced approximately 2 mm from its best focus position in order to obtain a more linear output. This displacement led to a beam spot size of 70 μm inside the crystal which although reduced the slope efficiency to 23%, it also slightly improved the stability of the system due to reduced thermal effects (Figure 5.8.b). This behavior is caused by the uneven beam spot size in the laser crystal resulting from the usage of the 100 μm fiber

44

core. Since the diffraction effect becomes more severe with smaller apertures, using a 100 μm fiber with the laser diode led to a large diffraction effect when combined with the strong focusing optics. With the pump source that was coupled with a 200 μm core fiber, the same setup gave a linear set of output powers as can be seen in Figure 5.8.c. It can also be noted that the slope efficiency obtained is also considerably higher. However as this source was damaged throughout the evolution of the thesis, the 100 μm core fiber coupled laser diode was utilized from this point on. Therefore the resonator had to be designed such that it could cope with strong thermal effects resulting from the intense pump beam.
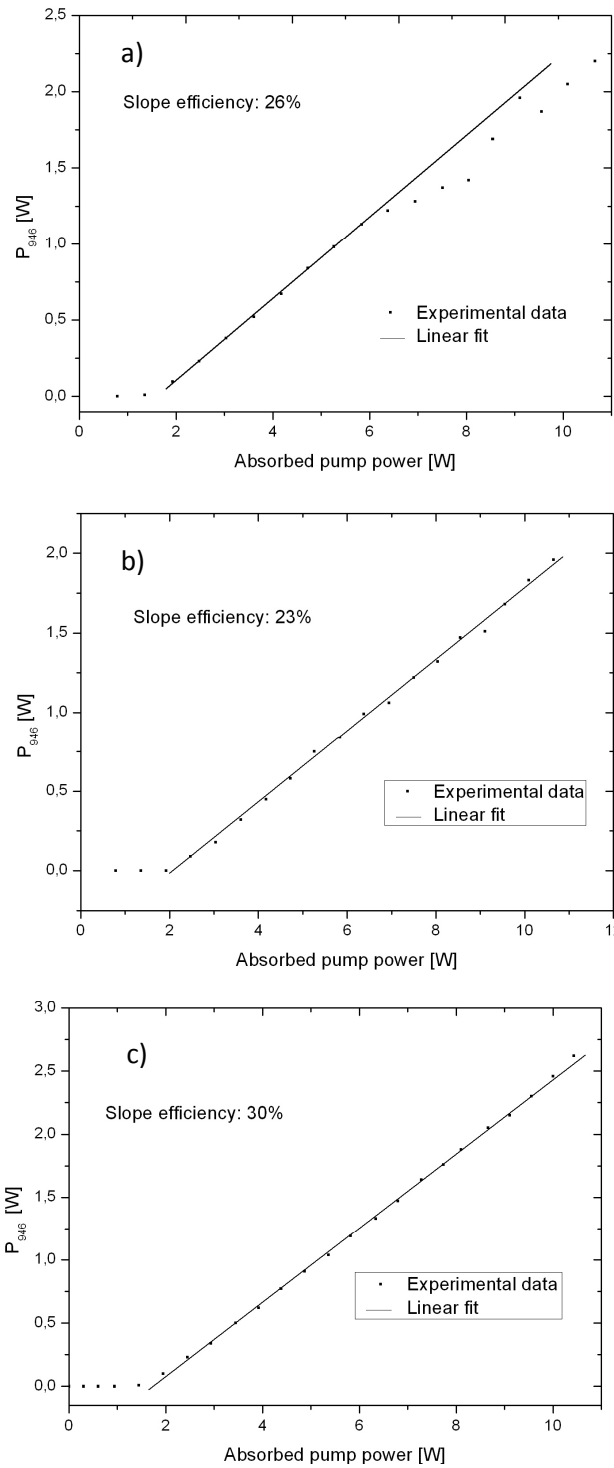
Figure 5.8 Absorbed pump power vs. laser power at 946 nm with a) 100 um fiber core source at best focus position b) after defocusing c) with 200 um fiber source.

5.2.1 Heat generation and thermal loading

Although end pumped configurations are advantageous in obtaining high conversion efficiencies and high quality laser modes, the powers obtained by such systems are limited due to thermal effects caused by tight focusing of the pump beam. Heat deposition in such configurations is inhomogeneous, leading to highly non-uniform temperature and stress profiles.

Mechanical Stress:

One consequence of such profiles is seen as mechanical stress in the crystal. Apart from causing possible fractures in the crystal the mechanical stress also induces small refractive index variations in the crystal via the photoelastic effect. This leads to birefringence in the crystal. When light is not polarized this does not cause any problems however for frequency conversion processes polarized light is required. The insertion of a polarizing element into the cavity in this case leads to depolarization losses. The light polarized by the polarizer will be divided into two orthogonal components due to the birefringence in the crystal. On its return path the stress induced orthogonally polarized portion of light will be rejected by the polarizer leading to losses. The effect of depolarization losses increase with pump power which in return reduces the efficiency[30]. The problem of stress induced birefringence becomes more severe in quasi-three level lasers. In such lasers higher pump intensities are required and also the low gain is strongly affected by the increases in resonator loss.

Thermal lensing effects:

Another result of temperature and stress variations exhibits itself as optical distortions. The tight focusing of the pump beam causes the gain medium to be hotter along the beam axis. As a result a transverse gradient of the refractive index is formed, leading to a thermal lensing effect of the active medium. The aberrated nature of the thermal lens leads to a degradation of the beam quality and also influences the resonator stability.
 It is more vital to compensate for the temperature increase in a quasi-three level system than a four level system since the reabsorption losses from the lower laser level increases with temperature. Also, because of the quasi-three level nature it is essential to focus the pump to a relatively small beam size due to low gain cross sections. This places extra demands on the resonator design which must cope with the resulting thermal effects. A number of temperature reduction techniques were used throughout this thesis in order to compensate for the thermal load which will now be discussed in further detail.

5.2.2 Effect of end Caps

In order to decrease thermal effects and enhance the performance of a solid-state laser, composite crystals can be utilized. Using such composite crystals with undoped end caps allows heat transfer from both faces of the Nd:YAG to the undoped YAG ends enlarging

the active material cooling surface. This in return reduces the reabsorption losses in the active segment which is strongly temperature dependant thereby improving the thermal uniformity of the laser active media The improvement of Nd:YAG laser performance by the use of composite rods was first demonstrated by Hanson[31] to obtain efficient room temperature pulsed operation at 946 nm and intracavity frequency doubling. It was shown that composite rods dramatically improve the output performance in such quasi-three level operation in Nd:YAG 946 nm.
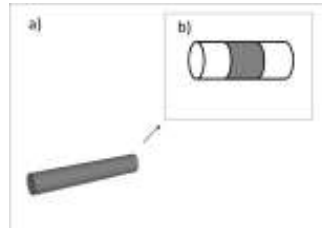

Figure 5.9 a) Nd:YAG crystal b) undoped-doped-undoped segments.

The heat arises from the radiationless transitions in the material i.e the energy differential from pump to fluorescent bands. When Nd:YAG is pumped by 808 nm laser diode radiation the heat losses reach at least 14.5% of the absorbed power caused by non-radiative transitions inside the doped part of the laser crystal. In the existence of ETU due to multi-phonon relaxations the heating of the crystal becomes more severe. Several studies[31],[32] have shown that the output power of the laser whose active material consists of a composite crystal reaches higher output powers than that of a system with conventional active medium design. The end caps provide efficient cooling leading to a more homogenous distribution of the thermal field in the doped part of the crystal.

5.2.3 Spatial Overlap of Pump and Laser Beam

Another design criterion that was taken into account in order to reduce thermal effects was spatial overlap between the pump radiation and the laser mode. This is more important in quasi-three level lasers due to the higher difficulty of achieving the laser threshold conditions. Having the laser mode size larger than the pump mode size, results in reabsorption to the upper laser level, leading to a loss in laser efficiency. Earlier studies by Pavel et al[33] have shown that the optimum ratio of an average pump size radius and laser beam radius ratio should be close to unity for an Nd:YAG crystal pumped at 10 W. In order to investigate correspondence of the laser mode with the pump mode computer simulation was used. Further discussion regarding this topic will be given in the next section concerning cavity simulation.

5.2.4 Winlase Cavity simulation

For designing a stable and efficient cavity supporting a single TEM_{00} mode, first a simulation was made using WinLase design program[34]. In making the simulation the mode size in the laser crystal with respect to the pump spot size was taken into

consideration. Although, according to the simulation, smaller radius of curvatures provided better spatial overlap between the pump and laser modes, it was observed experimentally that the amount of obtainable powers decreased with smaller ROC values (Figure 4.3). This is caused by the reduced laser mode sizes. As the laser mode size gets smaller the amount of energy that can be stored in the mode is reduced. Therefore a design was made which would compromise between getting a good spatial overlap and a relatively large laser mode. The laser mode size according to the simulation gave a value of approximately 100 μm. The resonator design was also made such that the strong thermal effects were stable over a wide range of thermal lens powers. This was especially important since reliable data for calculating the strength of the thermal lensing is often difficult to obtain. As a result a cavity length of 3.2 cm was chosen. The distances between cavity elements are given in Figure 5.1.

5.2.5 Water Cooling

A reduction of reabsorption loss without reducing the pump absorption can be achieved by decreasing the temperature of the laser rod. Effective removal of the heat can be accomplished by water cooling. In this thesis a water pump (Melcor Liquid Chiller) was used to cool the laser rod to a temperature of 13°C. Heat was extracted by direct contact with water from the side surface of the laser rod.

5.3 Q-switched operation at 946 nm

The Cr^{4+}:YAG sample used in this thesis was a thin AR coated (for 946 nm) disc with a thickness of 0.5 mm and an initial transmission of 94%. It was employed in the Brewster angle which resulted in a linearly polarized output with an extinction ratio of 100:1 at maximum power. When the Brewster plate was inserted in to the cavity to achieve polarized operation, a reduction of output powers was observed. At 1.5 W cw power at 946 nm it was seen that the output power reduced to 1 W after the insertion of the Brewster window. Shimony *et al.* accounts this for the additional residual absorption of the Q-switch plate under saturation conditions[20] i.e ESA. Depolarization losses mentioned earlier is also a possible loss factor leading to the observed reduction in the Q-switched average power.
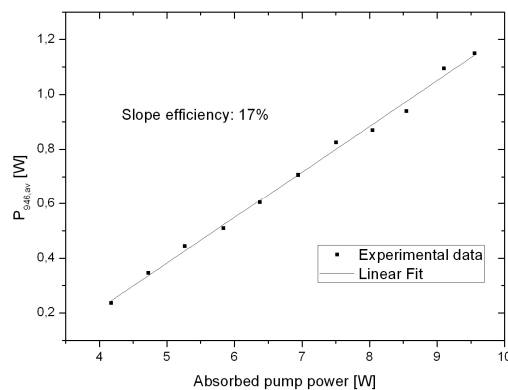

Figure 5.10 The 946 nm average power as a function of absorbed pump power.

The slope efficiency obtained was 17%. It was observed that increasing the value of absorbed power above 9 W caused damage in the Cr^{4+}:YAG. This was a limiting factor for the amount of power that could be pumped into the system. The resulting pulses were measured using a digital sampling oscilloscope. The pulse-width of a selected spike from the train was 12.4 ns (FWHM). The Q-switch repetition rate of the pulse train was 38 kHz. The repetition rates obtained varied between 9-42 kHz where the values increased with increased pump powers. The high repetition rates obtained were attributed to the tight focusing of the pump light in the crystal.
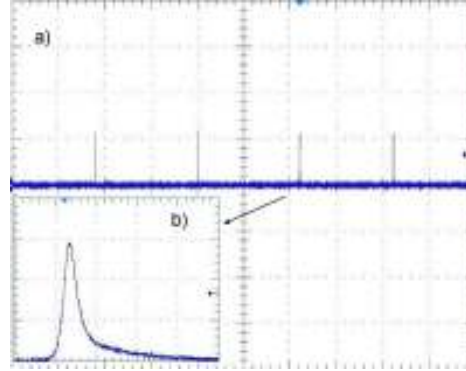

Figure 5.11 a) Pulse train of Q-switched emission at 946 nm b) seleceted single pulse

At 9 W of absorbed pump power a linearly polarized avarge power of 1 W was obtained. This corresponds to a pulse energy of 28.8 μJ and a peak power of 2.32 kW. The result was compared to the theoretical values of the Q-switched output pulse using an approach proposed by Xiao and Bass[35]. This model is based on Degnan analysis for optimization of passively Q-switched lasers [36] but is modified for taking ESA in the absorber into account. The total energy in the Q-switched pulse is given as [10]:

$$E = \frac{h\nu A}{2\sigma\gamma} \ln\left(\frac{1}{R}\right) \ln\left(\frac{n_i}{n_f}\right)$$

(5.1)

Where A is the effective cross section area of the laser beam in the laser medium, $h\nu$ is the laser photon energy, n_i and n_f are the initial and final population densities in the gain medium, R is the output coupler reflectivity and σ is the stimulated emission cross section of the laser rod. In order to solve this equation n_f and n_i were calculated by solving below equation[35]:

$$n_i - n_f - \frac{l_s\gamma}{l}\left(1 - \frac{\sigma_{es}}{\sigma_{gs}}\right) n_0 \left(1 - \left(\frac{n_f}{n_i}\right)^{\alpha'}\right)$$

(5.2)

$$- \frac{\left(\ln\left(\frac{1}{R}\right) + L + 2\sigma_{es}n_0l_s\right)}{2\sigma l} \ln\left(\frac{n_i}{n_f}\right) = 0$$

Here n_0 is total population density for the saturable absorber and can be found using the following expression[37]:

$$T_0 = exp(-n_0 l s)$$ (5.3)

where T_0 is the initial transmission and l_s is the thickness of the saturable absorber. The value for n_i can be found solving:

$$2\sigma n_i l - 2\sigma_{gs} n_0 l_s - \left(\ln\left(\frac{1}{R}\right) + L \right) = 0$$ (5.4)

	Parameter	Value
Nd:YAG	Crystal Length (l)	5 mm
	Spontaneous emission lifetime (τ)	230 us [10]
	Degeneracy factor γ	2
	Stimulated emission cross section (σ)	5.1×10^{-20} cm^2 [38]
Cr^{4+}:YAG	Crystal length	0.5 mm
	Initial transmission (T_0)	0.94
	Ground-state absorption cross section (σ_{gs})	4×10^{-18} cm^2 [39]
	Excited state absorption cross section (σ_{es})	1.1×10^{-18} cm^2 [39]
Output Couper reflectance	0.90	
Non saturable losses (L)	4.8%	

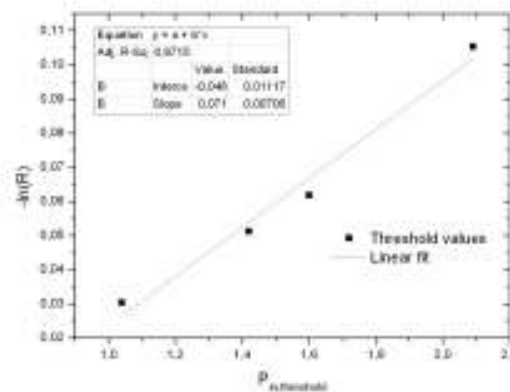Table 5.1 List of values used in the simulation

Figure 5.12 Findlay-Clay analysis where the intersection of the straight line indicates the losses in the system.

The value for linear losses was calculated using a standard Finlay-Clay analysis[40]. In doing this output mirrors with different reflectivity values were used in determining threshold powers for lasing for each mirror. Extrapolation of the straight line plot of $-lnR$ vs P_{th} at $P_{th} = 0$ yields the round trip resonator loss L. The value for L measured for this case was determined to be $L = 4.8\%$ as shown in Figure 5.12.

The measured value was modified taking ESA into account using:

$$L' = L + 2\sigma_{es}n_0l_s \tag{5.5}$$

This yielded a value of $L' = 6.1\%$ for the intrinsic losses in the system. In solving Eq.4.2 it is also necessary to introduce the constants γ and γ_s defined by Degnan. Here γ is the degeneracy factor which is 2 for quasi-three level lasers and γ_s defines the effect of the absorption of a single photon by the saturable absorber on the absorber population density. This value can be calculated using the below equation where again ESA has been taken into account[35]:

$$\gamma_s' = \frac{1}{1 - \dfrac{\sigma_{es}}{\sigma_{gs}}} \tag{5.6}$$

Here σ_{gs} and σ_{es} are the absorber ground-state and excited-state cross sections, respectively. The value for A was estimated using WinLase cavity simulation. The theoretical value obtained was 36 mJ of average power.

Insertion of the passive Q-switch element provided a better beam quality then the one obtained in the cw mode due to a shaping effect provided by the nonlinear saturation mechanism[41]. The Q-switched beam had an M^2 value of 1.9 in the x direction and 2.2 in the y direction.
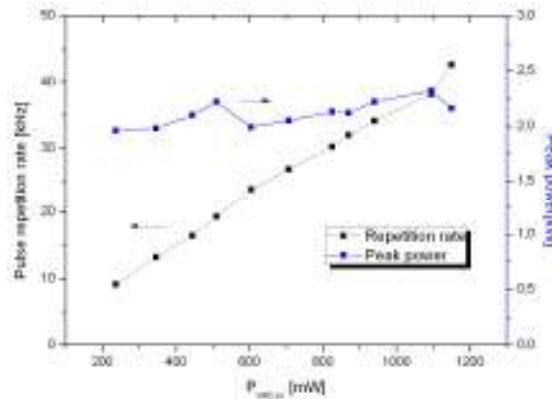

Figure 5.13 Pulse length and pulse energy as a function of 946 nm average power.
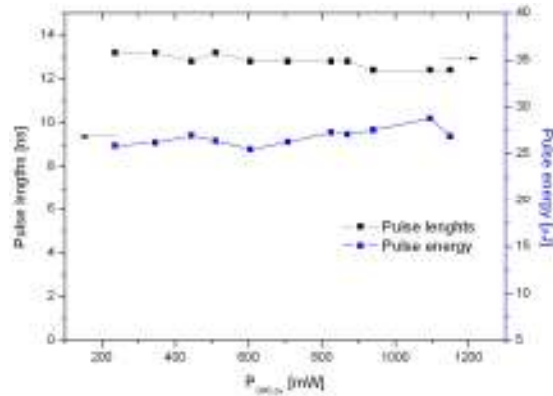
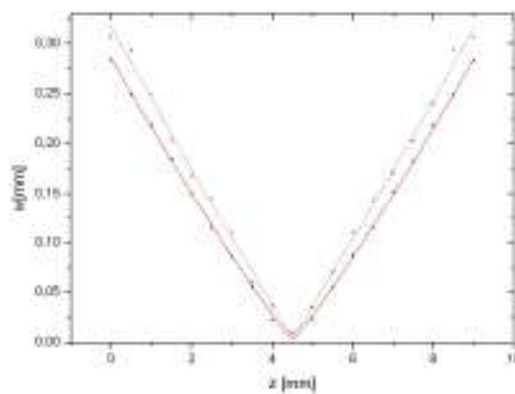*Figure 5.14 Pulse repetition rate and peak power as a function of 946 nm average power*

Figure 5.15 Beam waist vs. distance z where solid lines indicate y axis and dashed lines indicate x axis.

5.4 SHG using BiBO and PPKTP

The generation of second harmonic light at 473 nm was first obtained by frequency doubling in BiBO crystal (BiB$_3$O$_6$) cut for type-I phase-matching (ee->o). with θ = 161.7 and φ =90. BiBO has a high damage threshold and a high effective nonlinear coefficient value of 3.34 pm/V. In order to achieve second harmonic generation an extra-cavity configuration was utilized. This type of frequency doubling where the nonlinear crystal is placed outside the cavity has the advantages of good output mode, high stability and a simple optical system. However the obtainable conversion efficiencies are not as high as that of intra-cavity frequency doubling since it does not work in a resonant way. The crystal used for the SHG process had a length of 10 mm. It was AR coated for both 946 nm and 473 nm and was mounted onto a copper block cooled by a thermoelectric cooler (TEC). The temperature of the crystal was maintained at 22°C throughout the experiment. The 946 nm pulsed output was first collimated using a 100 mm focal length lens and focused into the BiBO crystal using a second lens with 75 mm focal length. The resulting beam waist had a 38 μm beam radius in the crystal. In order to filter out the IR from the generated blue a dichroic mirror was used. Figure 5.15 shows the average power obtained for 473 nm as a function of 946 nm peak power. The maximum conversion efficiency

53

reached was 8.4%. A theoretical analysis was held in order to compare the experimentally obtained result. The theoretical value obtained for the conversion efficiency was 14.1%
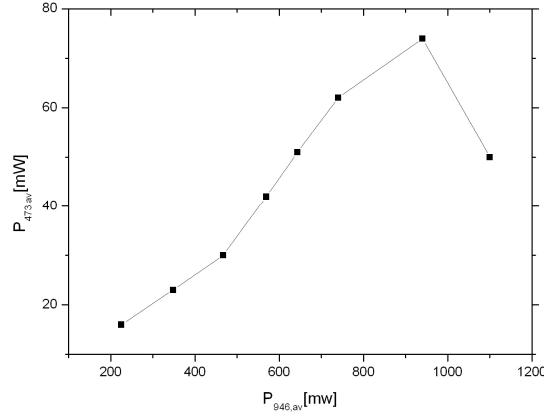

Figure 5.16 Avarage power at 473 nm as a function of $P_{946,av}$

It should be noted that when using such a setup with a single pass regime it is very important to optimize the fundamental beam focusing in order to obtain high conversion efficiencies. The optimum beam waist radius for a 10 mm crystal according to Boyd-Kleinman[22] criteria is 17 μm. The experimentally obtained beam waist would thus partially explain the low average blue power and the low conversion efficiency obtained. The pulse-width of the selected spike from the spiking train was 8.8 ns (FWHM) where the pulse train had a repetition frequency of 45 kHz. The large walk-off angle of the BiBO cyrtsal (0.65 mrad) causes the output blue beam to be elliptical.
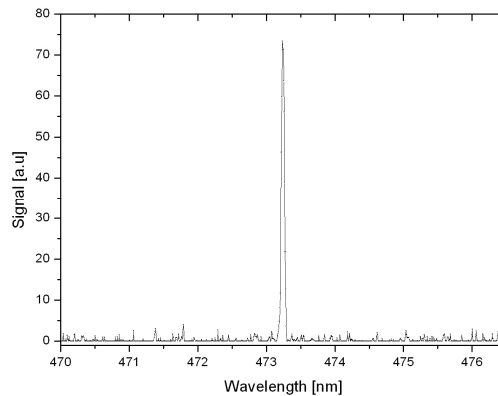

Figure 5.17 Measured emission spectrum at 473 nm

Blue generation was also obtained with a PPKTP crystal of 5 mm length. The value for the nonlinear coefficient d_{33} is 16.9 pm/V. Hence the theoretical value for d_{eff} becomes 9.8 pm/V[42]. The crystal had a poled period of 6.09 μm. The fundamental beam was focused to a spot size of 38 μm in the crystal. Due to possible damages that could result in KTP mentioned earlier in Section 4.5 a rather loose focusing was chosen. The pulse-width of the selected spike from the spiking train was 10.8 ns (FWHM) where the pulse

train had a repetition frequency of 43.6 kHz. An average power of 245 mW was observed at 0.94 W of pulsed fundamental input power at 946 nm. The result obtained at maximum average power for 473 nm was compared to a theoretically calculated value. The maximum conversion efficiency obtained was 26% as opposed to the theoretically calculated value of 47%.
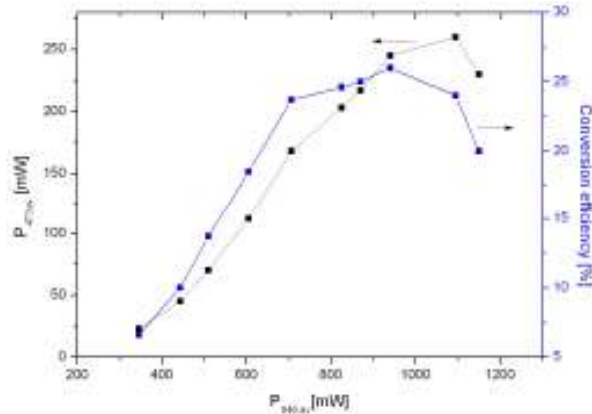

Figure 5.18 Average blue power and conversion efficiency at 473 nm with respect to average power at 946 nm.

For higher fundament powers a saturation effect, followed by a decrease was observed in the conversion efficiency. This can be explained by increased blue absorption in the rear part of the crystal. Apart from loss at 473 nm, this leads to temperature gradients and consequently, a refractive index change in the crystal. As a combined effect of the temperature variation this will lead to detuning from phase-matching. Photochromic effect in KTP will also lead to absorption in the infrared (BLIIRA) induced by the blue light as mention earlier in Section 4.5. Apart from having similar effects as mentioned above, this will reduce the available power for nonlinear conversion. Figure 5.19 displays the measured phase-matching curve for the 5 mm long PPKTP crystal. It can be seen that the measured phase-matching temperature T_0 was 22.5 ^{o}C and the FWHM temperature bandwidth ΔT_{FWHM} was 6.0 ^{o}C. The obtained curve is very close to a sinc^2-function however the two side of the peak is asymmetric which is also believed to be caused from the temperature gradients mentioned above. From the obtained results it was observed that PPKTP provided higher blue power than BiBO primarily due to its larger nonlinear coefficient.
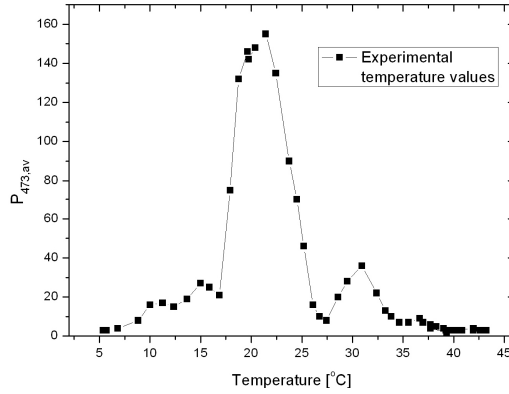
Figure 5.19 473 nm average power as a function og PPKTP crystal temperature, T_0 = 22 ^{o}C and ΔT_{FWHM} = 6.0^{o}C. The measurements were done using a 5 mm long PPKTP crystal (Λ = 6.09 μm) and a focused beam waist of 38 μm.

5.5 UV generation using BBO

The 473-nm light generated using the 5 mm long PPKTP crystal was frequency doubled a second time for UV generation at 236 nm. Again a single pass setup was used where this time a BBO (β-BaB$_2$O$_4$) crystal was utilized for type-I (oo->e) phase-matching (θ= 57.5^o). The crystal had dimensions of 3x3x3 mm^3 and was AR-coated for 473 nm and 236 nm. The phase-matching temperature was 23 ^{o}C and the nonlinear coefficient d$_{eff}$ was 1.5 pm/V. The generated blue was focused in to the BBO crystal using a collimation lens of 75 mm and a focusing lens of 25 mm in order to obtain a spot size of 18 μm. To separate the generated UV from the 473 emission a fused silica prism was utilized. Avarage UV power with respect to average power at 473 nm is given in Figure 5.20. The conversion efficiency did not exceed 1%.
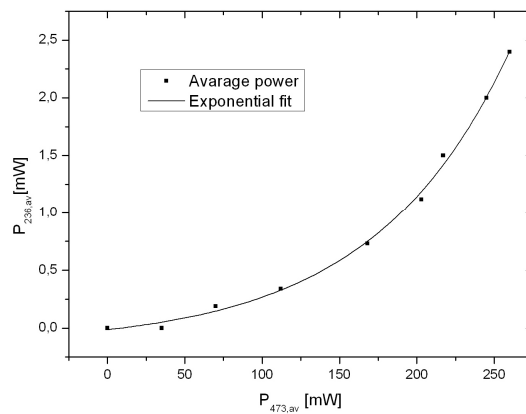

Figure 5.20 UV average power as a function of 473 nm average power.

Chapter 6: Conclusion and Outlook

In conclusion an all solid-state UV light source operating at a wavelength of 236 nm and an average power of 2.4 mW was designed and constructed. A Q-switched 946 nm laser with pulse rates between 9-42 kHz and 12.4 ns pulses was used as the fundamental source. Two different nonlinear crystals, BiBO and PPKTP were compared for the 473 nm second harmonic generation stage. A maximum of 260 mW of 473 nm was accomplished using the 5 mm long PPKTP crystal corresponding to a conversion efficiency of 26%. A way to optimize the output would be to increase the peak power generated from the Q-switched fundamental source. Constructing a setup with a better spatial overlap between the mode size and the pump spot size would be an important factor in this process. The result of poor overlap leads to reabsorption losses which in return reduce the laser efficiency. Also instabilities in the output power and degraded beam quality are observed in the case of too tight focusing. Another optimization step would be to use a shorter poling period, corresponding to higher phase-matching period. Since using KTP at elevated temperatures reduce the photochromic effect and lead to stable operation. Having optimum focusing conditions is also an important factor in obtaining increased conversion efficiency in SHG processes. It should also be noted that the damage threshold of Cr^{4+}:YAG is a limiting factor for the amount of power that could be pumped into the system. This drawback limited the results obtained in the generation of 473 nm and 236 nm light.

References

1. Maiman, T. H. "Stimulated Optical Radiation in Ruby." Nature 187, 493-494, 1960.

2. P. A. Franken, A. E. Hill, C. W. Peters, and G. Weinreich, Phys. Rev. Letters 7, 118 (1961) .

3. McClung, F.J. and Hellwarth, R.W, Journal of Applied Physics 33 3, 828-829 (1962).

4. Geusic, J.E., Marcos, H.M, and Van Uitert, L.G, Applied Physics Letters 4 10, 182-184 (1964).

5. O. Svelto, Principles of Lasers (University Science Books, California, 1986).

6. W.T. Silfvast, Laser Fundementals,1st Ed. Cambridge University Press, USA (2000).

7. J.S Kruger: Electro-Opt. System Design 12 (September 1971).

8. J.A. Arnaud, W.M. Hubbard, G.D. Mandeville, B. de la Claviere, E.A. Franke and J.M. Franke, Technique for fast measurement of laser beam parameters, Applied Optics 10 (1971), pp. 2775–2776.

9. T. Y. Fan and Robert L. Byer, Opt. Lett. 12, 809-811 (1987).

10. W.Koechner, Solid State Laser Engineering 5th edition (springer, Berlin, 1999).

11. Y.Guyot, H. Manan, J. Y. Rivoire, R. Maneorgé, N. Garnier, E. Deseroix, M. Bon, and P. Laporte, Phys. Rev. B 51, 784 (1995)

12. T. Chuang and H. R. Verdun, IEEE J. Quant. Electr. 32, 79 (1996).

13. S. Guy, C. L. Bonner, D. P. Shepard, D. C Hanna, A. C. Tropper, and B. Ferrand, IEEE J. Quant. Electr. 34, 900 (1998).

14. M. Pollnau, P. J. Hardman, W. A. Clarkson, and D. C. Hanna, Opt. Comm. 147, 203 (1998)

15. M. Pollnau, P. J. Hardman, M. A. Kern, W. A. Clarkson, and D. C. Hanna, Phys. Rev. B. 58, 16076 (1998)

16. P. J. Hardman, W. A. Clarkson, J. A. Friel, M. Pollnau, and D. C. Hanna, IEEE J. Quant. Electr. 35, 647 (1997)

17. W. G. Wagner and B.A. Lengyel, Journal of Applied Physics, 34, pp.2040-2046, July 1963.

18. A. Szabo, R.A. Stein: J. Appl. Phys. 36, 1562 (1965)

19. Agnesi A.; Dell'Acqua S.; Reali G.C; Sun ,Opt. and Quantum El. Volume 29, Number 3, (1997)

20. Y. Shimony, Z. Burshtein and Y. Kalisky, IEEE Journal Of Quantum Electronic, Vol. 31, No. 10, Oct. 1995.

21. Y. Shimony, Y. Kalisky and B.H.T. Chai, Opt. Mater. 4 (1995), p. 547

22. D.A Kleinman, Phys. Rev. 126, 1977 (1962)

23. G. D. Boyd and D. A. Kleinman, J. Appl. Phys. 39, 3597–363, 1968.

24. Richard L. Sutherland, Handbook of Nonlinear Optics, Marcel Dekker, New York (1996).

25. J.A.Armstrong,N. Blombergen,J.Ducuing, and P.S Pershan, Phys. Rev, 127,1918(1962)

26. M. M. Fejer, G. A. Magel, D. H. Jundt, and R. L. Bayer. IEEE J. Quant. Electron. 28 (1992)

27. Hirohashi, J.; Pasiskevicius, V.; Wang, S.; Laurell, F.,Journal of Applied Physics, Vol. 101, Issue 3, pp. 033105-033105-5 (2007).

28. S. Wang, V. Pasiskevicius and F. Laurell, J. Appl. Phys. 96 (2004), p. 2023

29. V. Pasiskevicius, H. Karlsson, F. Laurell, R. Butkus, V. Smilgevicius, and A. Piskarskas, Opt. Lett. 26, 710-712 (2001)

30. W. A. Clarkson, N. S. Felgate, and D. C. Hanna, Opt. Lett. 24, 820-822 (1999)

31. F. Hanson, Appl. Phys. Lett. 66, 3549–3551 (1995)

32. Masaki Tsunekane, Noboru Taguchi, and Humio Inaba, Appl. Opt. 37, 5713-5719 (1998)

33. N. Pavel, T. Taira: Opt. Eng. 38, 1806 (1999)

34. http://www.winlase.com/

35. G. Xiao and M. Bass, IEEE J. Quantum Electronics, Vol. 33, No. 1,(1997)

36. J. J. Degnan, IEEE J. Quantum Electronics, vol. 31, pp. 1890-. 1901,1995.

37. Z. Burshtein, P. Blau, Y. Kalisky, Y. Shimony, and M. R. Kokta, Quantum Electronics,34 (1998)

38. Singh, R. G. Smith, and L. G. Van Uitert, Phys. Rev. B. 10, 2566 (1974)

39. X.Zhang, A.Brenier, J.Wang, H.Zhang, Opt. Mater. 26, 293-296 (2004).

40. D. Findlay and R.A. Clay, Phys. Lett., 20, 277 (1966).

41. Agnesi A., Dell'Acqua S., Reali G.C., Optics Communications, Volume 133, Number 1, 1 January 1997 , pp. 211-215(5)

42. Sandra Johansson, Stefan Bjurshagen, Carlota Canalias, Valdas Pasiskevicius, Fredrik Laurell, and Ralf Koch, Opt. Express 15, 449-458 (2007)